Monthly Notices
of the
ROYAL ASTRONOMICAL SOCIETY

Mon. Not. R. Astron. Soc. **416,** 2640–2668 (2011) doi:10.1111/j.1365-2966.2011.19217.x

Galaxy and Mass Assembly (GAMA): the GAMA galaxy group catalogue (G^3Cv1)

A. S. G. Robotham,[1⋆] P. Norberg,[2] S. P. Driver,[1,3] I. K. Baldry,[4] S. P. Bamford,[5] A. M. Hopkins,[6] J. Liske,[7] J. Loveday,[8] A. Merson,[9] J. A. Peacock,[2] S. Brough,[6] E. Cameron,[10] C. J. Conselice,[5] S. M. Croom,[11] C. S. Frenk,[9] M. Gunawardhana,[11] D. T. Hill,[1] D. H. Jones,[12] L. S. Kelvin,[1] K. Kuijken,[13] R. C. Nichol,[14] H. R. Parkinson,[2] K. A. Pimbblet,[12] S. Phillipps,[15] C. C. Popescu,[16] M. Prescott,[4] R. G. Sharp,[17] W. J. Sutherland,[18] E. N. Taylor,[11] D. Thomas,[14] R. J. Tuffs,[19] E. van Kampen[7] and D. Wijesinghe[11]

[1]*Scottish Universities Physics Alliance (SUPA), School of Physics and Astronomy, University of St Andrews, North Haugh, St Andrews KY16 9SS*
[2]*Scottish Universities Physics Alliance (SUPA), Institute for Astronomy, University of Edinburgh, Royal Observatory, Blackford Hill, Edinburgh EH9 3HJ*
[3]*International Centre for Radio Astronomy Research (ICRAR), The University of Western Australia, 35 Stirling Highway, Crawley, WA 6009, Australia*
[4]*Astrophysics Research Institute, Liverpool John Moores University, Egerton Wharf, Birkenhead CH41 1LD*
[5]*Centre for Astronomy and Particle Theory, University of Nottingham, University Park, Nottingham NG7 2RD*
[6]*Australian Astronomical Observatory, PO Box 296, Epping, NSW 1710, Australia*
[7]*European Southern Observatory, Karl-Schwarzschild-Str. 2, 85748 Garching, Germany*
[8]*Astronomy Centre, University of Sussex, Falmer, Brighton BN1 9QH*
[9]*Institute for Computational Cosmology, Department of Physics, Durham University, South Road, Durham DH1 3LE*
[10]*Department of Physics, Swiss Federal Institute of Technology (ETH-Zürich), 8093 Zürich, Switzerland*
[11]*Sydney Institute for Astronomy, School of Physics, University of Sydney, NSW 2006, Australia*
[12]*School of Physics, Monash University, Clayton, Victoria 3800, Australia*
[13]*Leiden University, PO Box 9500, 2300 RA Leiden, the Netherlands*
[14]*Institute of Cosmology and Gravitation (ICG), University of Portsmouth, Dennis Sciama Building, Portsmouth PO1 3FX*
[15]*HH Wills Physics Laboratory, University of Bristol, Tyndall Avenue, Bristol BS8 1TL*
[16]*Jeremiah Horrocks Institute, University of Central Lancashire, Preston PR1 2HE*
[17]*Research School of Astronomy and Astrophysics, Mount Stromlo Observatory, Cotter Road, Western Creek, ACT 2611, Australia*
[18]*Astronomy Unit, Queen Mary University London, Mile End Road, London E1 4NS*
[19]*Max Planck Institute for Nuclear Physics (MPIK), Saupfercheckweg 1, 69117 Heidelberg, Germany*

Accepted 2011 June 8. Received 2011 June 8; in original form 2011 April 28

ABSTRACT

Using the complete Galaxy and Mass Assembly I (GAMA-I) survey covering $\sim$142 deg^2 to $r_{\rm AB} = 19.4$, of which $\sim$47 deg^2 is to $r_{\rm AB} = 19.8$, we create the GAMA-I galaxy group catalogue (G^3Cv1), generated using a friends-of-friends (FoF) based grouping algorithm. Our algorithm has been tested extensively on one family of mock GAMA lightcones, constructed from Λ cold dark matter N-body simulations populated with semi-analytic galaxies. Recovered group properties are robust to the effects of interlopers and are median unbiased in the most important respects. G^3Cv1 contains 14 388 galaxy groups (with multiplicity $\geq$2), including 44 186 galaxies out of a possible 110 192 galaxies, implying $\sim$40 per cent of all galaxies are assigned to a group. The similarities of the mock group catalogues and G^3Cv1 are multiple: global characteristics are in general well recovered. However, we do find a noticeable deficit in the number of high multiplicity groups in GAMA compared to the mocks. Additionally, despite exceptionally good local spatial completeness, G^3Cv1 contains significantly fewer compact groups with five or more members, this effect becoming most evident for high multiplicity systems. These two differences are most likely due to limitations in the physics included of the current GAMA lightcone mock. Further studies using a variety of galaxy formation models are required to confirm their exact origin. The G^3Cv1 catalogue will be made publicly available as and when the relevant GAMA redshifts are made available at http://www.gama-survey.org.

Key words: galaxies: groups: general – galaxies: haloes – dark matter – large-scale structure of Universe.

⋆E-mail: asgr@st-and.ac.uk

1 INTRODUCTION

Galaxy group and cluster catalogues have a long history in astronomy. Early attempts at creating associations of galaxies were quite qualitative in nature (e.g. Abell 1958; Zwicky, Herzog & Wild 1961), but more recently significant effort has been devoted to robustly detecting grouped structures (e.g. Huchra & Geller 1982; Moore, Frenk & White 1993; Eke et al. 2004a; Gerke et al. 2005; Yang et al. 2005; Berlind et al. 2006; Brough et al. 2006; Knobel et al. 2009). The pioneering application of this process was by Huchra & Geller (1982), where the catalogue of De Vaucouleurs (1975), the earliest reasonably complete attempt at a group catalogue, was reconstructed using fully quantitative means – i.e. by a method that was reproducible and not subjective.

The power of group catalogues resides in their relation to the theoretically motivated dark matter (DM) haloes. Λ cold dark matter (ΛCDM), the literatures current favoured structure formation paradigm, makes very strong predictions about the self-similar hierarchical merging process that occurs between haloes of DM (Springel et al. 2005). Galaxy groups are the observable equivalent of DM haloes, and thus offer a direct insight into the physics that has occurred in the DM haloes in the Universe up to the present day. Further to offering a route to studying DM dynamics (e.g. Plionis, Basilakos & Ragone-Figueroa 2006; Robotham, Phillipps & De Propris 2008), analysis of galaxy groups opens the way to understanding how galaxies populate haloes (e.g. Cooray & Sheth 2002; Yang, Mo & van den Bosch 2003; Cooray 2006; Robotham et al. 2006; Robotham, Phillipps & De Propris 2010b).

The strongest differentials between competing physical models of DM are found at the extremes of the halo mass function (HMF), i.e. on cluster scales (e.g. Eke, Cole & Frenk 1996) and on low mass scales. The HMF describes the comoving number density distribution of DM haloes as a function of halo mass. Low-mass groups are highly sensitive to the temperature of the CDM. We either expect to see a continuation of the near power-law prediction for the HMF down to Local Group mass haloes (see Jenkins et al. 2001, and references therein) for a CDM Universe, or, as the DM becomes warmer, the slope should become suppressed significantly.

The Galaxy and Mass Assembly project (GAMA) is a major new multiwavelength spectroscopic galaxy survey (Driver et al. 2011). The final redshift survey will contain $\sim$400 000 redshifts to $r_{\rm AB} = 19.8$ over $\sim$360 deg^2, with a survey design aimed at providing an exceptionally uniform spatial completeness (Baldry et al. 2010; Robotham et al. 2010a; Driver et al. 2011). One of the principal science goals of GAMA is to make a statistically significant analysis of low-mass groups ($M \leq 10^{13}\,h^{-1}\,{\rm M}_{\odot}$), helping to constrain the low-mass regime of the DM HMF and galaxy formation efficiency in Local Group like haloes.

As well as allowing us to determine galaxy group dynamics and composition at the highest fidelity possible due to the increased redshift density, GAMA will also provide multiband photometry spanning the ultraviolet [UV; *Galaxy Evolution Explorer* (*GALEX*)], visible [Sloan Digital Sky Survey (SDSS), VLT Survey Telescope (VST)-Kilo-Degree Survey (KIDS)], near-infrared [IR; UKIRT Infrared Deep Sky Survey (UKIDSS)-Large Area Survey (LAS), VISTA Kilo-degree Infrared Galaxy (VIKING)], mid-IR [*Wide-field Infrared Survey Explorer* (*WISE*)], far-IR [Australia Telescope Large Area Survey (ATLAS)] and radio [Giant Metrewave Radio Telescope (GMRT), Australian Square Kilometre Array Pathfinder (ASKAP)]. By combining a GAMA galaxy group catalogue (G^3Cv1) constructed with spatially near-complete redshifts and 21 band photometry, the GAMA project is in a unique position to answer many of the most pressing questions that exist in extragalactic astronomy today. Crucially, the interplay between star formation rate (SFR), stellar mass, morphology, quasi-stellar object (QSO) activity and star formation efficiency (SFE) with environment can be probed in unprecedented detail. The group catalogue presented here will also enable galaxy evolution to be investigated as a function of halo mass, rather than with coarse environmental markers, in statistically significant low-mass regimes for the first time. This is a huge advance on the capabilities of current large spectroscopic surveys like SDSS and Two-degree-Field Galaxy Redshift Survey (2dFGRS) that are almost single pass and hence suffer seriously from spectroscopic incompleteness in clustered regions. GAMA, by being at least six pass in every unit of sky, is exceptionally complete on all angular scales (Robotham et al. 2010a; Driver et al. 2011).

The catalogue and group analyses presented here are based on the first three years of spectroscopic observations (2008 February to 2010 May) made at the Anglo-Australian Telescope (AAT). Within the GAMA project, this period is referred to as GAMA-I, since the deeper, larger area, continuation of the GAMA survey is commonly referred to as GAMA-II.

The paper is organized as follows. Section 2 describes the precise friends-of-friends (FoF) grouping algorithm, the GAMA data and the lightcone mocks used for the present analysis. The testing and grouping parameter optimization using the mocks are considered in Section 3. Group properties (i.e. velocity dispersion, radius, dynamical mass and total luminosity) and their estimates are presented in Section 4. Section 5 presents global group properties for G^3C and corresponding mock group catalogues. A few GAMA group examples are discussed in Section 6, with conclusions presented in Section 7. We assume throughout an $\Omega_{\rm m} = 0.25$, $\Omega_{\Lambda} = 0.75$, $H_0 = h\,100\,{\rm km\,s^{-1}\,Mpc^{-1}}$ cosmological model, corresponding to the cosmology of the Millennium N-body simulation used to construct the GAMA lightcone mocks.

2 GALAXY GROUPING: ALGORITHM, DATA AND MOCKS

There are many subtle differences in the specific algorithm used to construct groups from spectroscopic surveys, but the major dichotomy occurs at the scale of association considered: galaxy–galaxy links or halo–galaxy links. Here we adopt galaxy–galaxy linking via a FoF algorithm (Section 2.1), having also explored a halo–galaxy grouping and found it to be less successful at recovering small-mass groups from our mock galaxy catalogues. The halo method implemented was a variant of the Voronoi tessellation scheme used in Gerke et al. (2005), which worked reasonably well for larger groups and clusters, but was not competitive compared to our FoF implementation in the low halo mass regime.

2.1 Friends of friends

A standard FoF algorithm creates links between galaxies based on their separation as a measure of the local density. In practice the projected and radial separations are treated separately, due to significant line-of-sight effects from peculiar velocities within groups and clusters. The comoving radial separations within a group appear larger than the projected ones, because radial distances inferred from galaxy redshifts contain peculiar velocity information along the line of sight on top of their underlying Hubble distance away from the observer. Fig. 1 shows schematically how the radial and projected separations are used to detect a group. This shows that

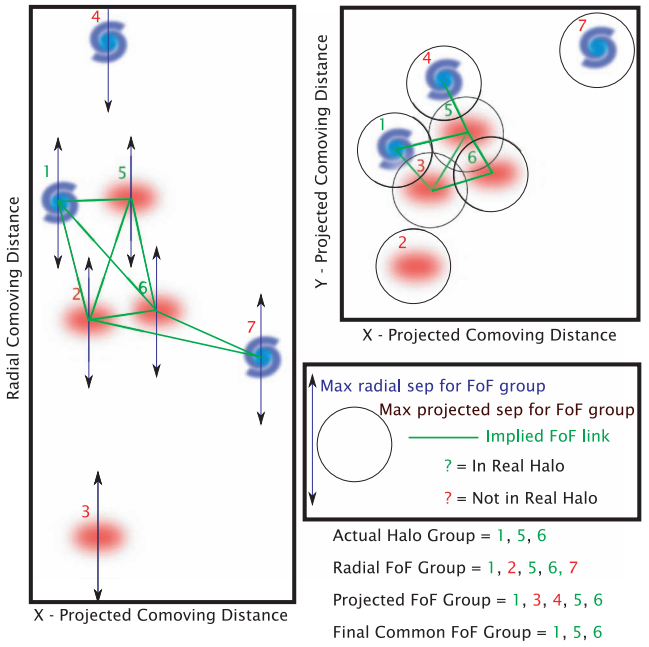

Figure 1. Schematic of the two-step process used when associating galaxies via FoF algorithm on redshift survey data. The same set of galaxies are shown in two panels: along the line of sight (left) and projected on the sky (right). Both the radial and projected separations are used to disentangle projection effects and recover the underlying group (galaxies 1, 5 and 6 in this example). The radial linking length has to be significantly larger than the projected one to properly account for peculiar velocities along the line of sight.

neither the radial nor the projected separation provides enough information to unambiguously detect a group, but their combination generate a secure grouping.

2.1.1 *Projected linking condition*

In its simplest form we can say that two galaxies are associated in projection when the following condition is met:

$$\tan[\theta_{1,2}](D_{\rm com,1} + D_{\rm com,2})/2 \leq b_{i,j}(D_{\rm lim,1} + D_{\rm lim,2})/2, \quad (1)$$

where $\theta_{1,2}$ is the angular separation of the two galaxies, $D_{{\rm com},i}$ is the radial distance in comoving coordinates to galaxy i, $b_{i,j}$ the mean required linking overdensity and $D_{{\rm lim},i}$ is the mean comoving intergalaxy separation at the position of galaxy i, here defined as

$$D_{{\rm lim},i} = \left[\int_{-\infty}^{M_{{\rm lim},i}} \phi(M)\,{\rm d}M\right]^{-1/3}, \quad (2)$$

where $M_{{\rm lim},i}$ is the effective absolute magnitude limit of the survey at the position of galaxy i, $\phi(M)$ the survey galaxy luminosity function (LF).

b is used to specify the overdensity with respect to the mean required to define a group. The approximate overdensity contour that this linking would recover in a simulation (Universe) with equal mass particles (galaxies) is given by $\rho/\bar{\rho} \sim 3/(2\pi b^3)$ (Cole & Lacey 1996). For a uniform spherical distribution of mass the virial radius corresponds to a mean overdensity of 178, hence the popularity of masses defined as being within 178 and 200 times the mean overdensity. For an NFW-type profile (Navarro, Frenk & White 1996) the overdensity within the virial radius is approximately 178/3 $\simeq$ 59. This implies an interparticle linking length of $b \simeq 0.2$ in real space, corresponding to a volume overdensity $1/b^3 = 125$ between galaxies. Linking together 1000s of DM particles in a simulation with real-space coordinates is a relatively simple and robust process, extending this methodology to redshift space using galaxies that trace the DM is non-trivial. Consequently, it is not simply true to state that $b = 0.2$ will return the virial mass limits for each galaxy group in the GAMA catalogue. Instead, b will be recovered from careful application to mock catalogues (see below for full details). Since there a subtle effects that vary the precise b used on a galaxy by galaxy basis $b_{i,j}$ used above is the mean b for galaxy i and j, respectively. In general, for near-by galaxies, b does not vary significantly.

To this standard form of the mean comoving intergalaxy separation at the position of galaxy i, we introduce an extra term, with equation (2) thus becoming

$$D_{{\rm lim},i} = \left(\frac{\phi(M_{{\rm lim},i})}{\phi(M_{{\rm gal},i})}\right)^{\nu/3} \left[\int_{-\infty}^{M_{{\rm lim},i}} \phi(M)\,{\rm d}M\right]^{-1/3}, \quad (3)$$

where $M_{{\rm gal},i}$ is the absolute magnitude of galaxy i. This extra term, $(\phi(M_{{\rm lim},i})/\phi(M_{{\rm gal},i}))^{\nu/3}$, allows for larger linking distances for intrinsically brighter galaxies, provided $\nu > 0$ and the LF is strictly increasing (which is true for GAMA). Adjusting ν allows the algorithm to be more or less sensitive to the intrinsic brightness of a galaxy, and can be thought of as a softening power. The principle behind introducing this term is that associations should be more significant between brighter galaxies, and tests on mocks show that this generates notably better quality group catalogues as determined from the cost function (see Section 3.1).

2.1.2 *Line-of-sight linking condition*

With equation (1) we have established an association in projection, but we also require that a given pair of galaxies are associated along the line of sight or radially, i.e.

$$|D_{\rm com,1} - D_{\rm com,2}| \leq b\,R\,(D_{\rm lim,1} + D_{\rm lim,2})/2, \quad (4)$$

where b is the linking length of equation (1), $D_{{\rm lim},i}$ is given by equation (3) and R is the radial expansion factor to account for peculiar motions of galaxies within groups. With a redshift survey, the measured redshift contains both information on the Hubble flow redshift and any galaxy peculiar velocity along the line of sight.

2.1.3 *Global linking conditions*

To construct a group catalogue we link together all associations that meet our criteria given by equations (1) and (4). Galaxies that are not directly linked to each other can still be grouped together by virtue of common links between them. All possible groups are constructed in precisely this manner, leaving either completely ungrouped galaxies or galaxies in groups with two or more members.

Despite its apparent simplicity, a FoF algorithm is still a very parametric approach to grouping. On top of the assumed cosmology, it requires the survey selection function, and values for the linking parameters b and R. The galaxy LF can be directly estimated from the data (e.g. Loveday et al. 1995; Norberg et al. 2002; Blanton et al. 2003), while the linking parameters cannot be estimated from the data. Instead they are commonly determined from either analytic calculations or analyses of N-body simulations populated with galaxies, with the latter approach taken here (see Section 2.3 for the description of the GAMA lightcone mocks).

Merely using a static combination of b and R is less than optimal for accurately reconstructing groups in the mock data. An obvious

shortcoming is that galaxies in clusters are significantly spread out along the line of sight, due to their large peculiar velocities a result of being bound to massive structures. To account for this we introduce a local environment measure that calculates the density contrast of a cylinder that is centred on the galaxy of interest. Similar to the approach of Eke et al. (2004a), we allow the b and R parameters to scale as a function of the observed density contrast, leading to position ($\boldsymbol{r}$) and faint magnitude limit ($m_{\rm lim}$)-dependent linking parameters:

$$b(\boldsymbol{r}, m_{\rm lim}) = b_0 \left(\frac{1}{\Delta} \frac{\rho_{\rm emp}(\boldsymbol{r}, m_{\rm lim})}{\bar{\rho}(\boldsymbol{r}, m_{\rm lim})} \right)^{E_b}, \quad (5)$$

$$R(\boldsymbol{r}, m_{\rm lim}) = R_0 \left(\frac{1}{\Delta} \frac{\rho_{\rm emp}(\boldsymbol{r}, m_{\rm lim})}{\bar{\rho}(\boldsymbol{r}, m_{\rm lim})} \right)^{E_R}, \quad (6)$$

where $\bar{\rho}$ is the average local density implied by the selection function, $\rho_{\rm emp}$ is the empirically estimated density, $m_{\rm lim}$ the apparent magnitude limit at position $\boldsymbol{r}$ and Δ is the density contrast, an additional free parameter together with E_b and E_R. For this work $\bar{\rho}$ is estimated from the galaxy selection function at $\boldsymbol{r}$ (i.e. it varies with the GAMA survey depth). $\rho_{\rm emp}$ is calculated directly from the number density within a comoving cylinder centred on $\boldsymbol{r}$ and of projected radius r_Δ and radial extent l_Δ. Δ determines the transition between where the power scaling reduces or increases the linking lengths, so a galaxy within a local volume precisely Δ times overdense will not have its links altered. The exact values for E_b, E_R and Δ are determined from the joint optimization of the group cost function (see Section 3.1) for all the parameters that affect the quality of the grouping when tested on the mocks. The parameters required for the FoF algorithm described above are now $b_0, R_0, \Delta, r_\Delta, l_\Delta, E_b, E_R$ and ν. Whilst many parameters, b_0 and R_0 are the dominant one for the grouping, the latter six merely determining how best to modify the linking locally, and typically introducing minor perturbations to the grouping.

2.1.4 Completeness corrections

Since the GAMA survey is highly complete (∼98 per cent within the r-band limits) the effect of incompleteness is minor, and tests on the mocks indicate the final catalogues are extremely similar regardless of whether the linking length is adjusted based on the local completeness. A number of definitions of local completeness were investigated: completeness within a pixel on a mask, completeness on a fixed angular top-hat scale around each galaxy and a completeness window function that represents the physical scale of a group on the sky. The difference between each was quite minor, but defining completeness on a physical scale produced marginally better grouping costs (Section 3.2). Hence the completeness corrected linking parameter b at position $\boldsymbol{r}$ is given by

$$b_{\rm comp}(\boldsymbol{r}, m_{\rm lim}) = \frac{b(\boldsymbol{r}, m_{\rm lim})}{c(\boldsymbol{r})^{1/3}}, \quad (7)$$

where $c(\boldsymbol{r})$ is the redshift completeness within a projected comoving radius of $1.0\,h^{-1}$ Mpc centred on $\boldsymbol{r}$. The effect is to slightly increase the linking length to account for the loss of (possible) nearby galaxies that it could otherwise be linked with. Since GAMA was designed to be extremely complete even at small angular scales (Robotham et al. 2010a), the mean modifications are less than 1 per cent.

2.2 Data: GAMA survey

Extensive details of the GAMA survey characteristics are given in Driver et al. (2011), with the survey input catalogue described in Baldry et al. (2010) and the spectroscopic tiling algorithm in Robotham et al. (2010a).

Briefly, the GAMA-I survey covers three regions each $12^\circ \times 4^\circ$ centred at $09^{\rm h}$, $12^{\rm h}$ and $14^{\rm h}30^{\rm m}$ (respectively G09, G12 and G15 from here). The survey depths and areas relevant for this study are ∼96 deg^2 to $r_{\rm AB} = 19.4$ (G09 and G15) and ∼47 deg^2 to $r_{\rm AB} = 19.8$ (G12).[1] All regions are more than 98 per cent complete (see Driver et al. 2011, for precise completeness details), with special emphasis on a high close pair completeness, which is greater than 95 per cent for all galaxies with up to five neighbours within 40 arcsec of them (see fig. 19 of Driver et al. 2011).[2] Despite this high global redshift completeness, we still apply completeness corrections to the FoF algorithm (as described in Section 2.1) and use the masks described in Baldry et al. (2010) and Driver et al. (2011), to account for areas masked out by bright stars, poor imaging, satellite trails, etc. The velocity errors on GAMA redshifts are typically ∼50 km s^{-1} (Driver et al. 2011), slightly larger than the nominal SDSS velocity uncertainties of ∼35 km s^{-1} but significantly better than the typical ∼80 km s^{-1} associated with 2dFGRS redshifts (Colless et al. 2001).

For this study, we use a global GAMA ($k + e$)-correction of the form

$$(k + e)(z) = \sum_{i=0}^{N} a_i(z_{\rm ref}, z_{\rm p})(z - z_{\rm p})^i + Q_{z_{\rm ref}}(z - z_{\rm ref}), \quad (8)$$

where $z_{\rm ref}$ is the reference redshift to which all galaxies are ($k + e$)-corrected, $Q_{z_{\rm ref}}$ is a single luminosity evolution parameter (as in e.g. Lin et al. 1999), $z_{\rm p}$ is a reference redshift for the polynomial fit to median KCORRECT-v4.2 k-correction (Blanton & Roweis 2007) of GAMA-I galaxies and $a_i(z_{\rm ref}, z_{\rm p})$ the coefficients of that polynomial fit. The present study uses $z_{\rm ref} = 0$, $Q_0 = 1.75$, $z_{\rm p} = 0.2$ and $N = 4$, with $a = 0.2085, 1.0226, 0.5237, 3.5902, 2.3843$, for both data and mocks. The precise value for $Q_0 = 1.75$ is not essential, as our estimate of the LF accounts for any residual redshift evolution.

Once the global ($k + e$)-correction have been defined, it is straightforward to estimate the redshift-dependent galaxy LF using a non-parametric estimator like the stepwise maximum likelihood (SWML) of Efstathiou, Ellis & Peterson (1988). We perform this analysis in five disjoint redshift bins, which are all correlated through the global normalization constraint. This is set by the cumulative number counts at $r_{\rm AB} = 19.8$ (∼1050 galaxies deg^{-2}), as estimated directly from the full GAMA survey and compared to ∼6250 deg^2 of SDSS Data Release 6 (DR6) survey (to account for possible sample variance issues). This LF estimate is used both to described the survey selection function (as required by equations 1–6) to adjust the galaxy magnitudes in the GAMA mock catalogues (see Section 2.3) and is hereafter referred to as $\phi_{\rm GAMA}$.

2.3 GAMA mock catalogues

To appropriately test the quality and understand the intrinsic limitations of a given group finder it is essential to test it thoroughly on a series of realistic mock galaxy catalogues, for which the true grouping is known. Those tests should include all the limitations of the real spectroscopic survey, e.g. spectroscopic incompleteness, redshift uncertainties, varying magnitude limits, etc.

[1] See Baldry et al. (2010) for additional GAMA-I selections.
[2] 99.8 per cent of all galaxies have five or fewer neighbours within 40 arcsec.

In this first paper on GAMA groups, we limit our tests of the group finding algorithm to one single type of mock galaxy catalogue, constructed from the Millennium DM simulation (Springel et al. 2005), populated with galaxies using the GALFORM Bower et al. (2006) semi-analytic galaxy formation recipe. The galaxy positions are interpolated between the Millennium snapshots to best mimic the effect of a proper lightcone output, enabling the mocks to include the evolution of the underlying DM structures along the line of sight, key for a survey of the depth of GAMA that spans ∼4 Gyr. Finally, the semi-analytic galaxies have their SDSS *r*-band filter magnitudes modified to give a perfect match to the redshift-dependent GAMA luminosity and selection function (see Section 2.2; Loveday et al., in preparation). When adjusting the magnitudes, we use the global GAMA $k + e$-correction of equation (8). The nine mock galaxy catalogues have the exact GAMA survey geometry, with each mock extracted from the *N*-body simulation while preserving the true angular separation between the three GAMA regions.

The main limitations of this first generation of GAMA mock galaxy catalogue for the present group study are listed below.

(1) The luminosity-dependent galaxy clustering does not perfectly match the data (Kim et al. 2009), in particular in redshift space (Norberg et al., in preparation). By their nature, semi-analytic mock galaxy catalogue are not constrained precisely to match in any great detail the observed clustering signal [as opposed to halo occupation distributions (HOD) or conditional luminosity functions (CLF) mocks; e.g. Cooray & Sheth 2002; Yang et al. 2003; Cooray 2006].

(2) The GAMA survey is so spectroscopically complete to the GAMA-I survey limits (above 98 per cent on scales relevant for this study) that no attempt of modelling any residual survey incompleteness into the mocks have been made.

(3) Apparent magnitude uncertainties have a negligible effect on the GAMA survey selection and hence are not accounted for in these mocks.

(4) Velocity measurement uncertainties are not incorporated into the mocks.

(5) The nine GAMA mocks are not statistically independent, as they are drawn from a single *N*-body simulation. However, we ensure in the construction of the different mocks that no single galaxy at the exact same stage of evolution is found in more than one mock, i.e. there is no spatial overlap between the nine GAMA lightcone mocks created.

(6) Despite the high numerical resolution of the Millennium DM simulation, the lightcones used for this work, once the shift in magnitudes have been accounted for, are not complete below $M_{r_{\rm AB}} - 5\log_{10} h \simeq -14.05$. This limit is faint enough to not attempt to address this issue in this first generation of GAMA mocks.

(7) The halo definition used in these mocks correspond to standard halo definition of GALFORM (Cole et al. 2000; Bower et al. 2006; Benson & Bower 2010), i.e. DHalo (Helly et al. 2003), as listed in the Millennium GAVO data base.[3] DHalo is a collection of SubFind subhaloes (Springel et al. 2001) grouped together to make a halo. The differences between DHalo and FoFHalo[4] are subtle. A preliminary analysis on a small fraction of the mock data shows that the log ratio of the DHalo and FoFHalo masses are median unbiased, and exhibit a 1σ scatter of 0.05 dex. The 10 per cent population that exhibits the largest mass mismatch are still median unbiased (i.e. they will not affect the median relationship between the FoF masses we measure and the intrinsic DM mass of the halo), but can scatter more than 1 dex away from the median. Because the two halo mass definitions are not biased with respect to each other, the DHalo mass can be used safely in this paper as a halo mass definition.

(8) The most luminous galaxy of a halo is nearly always at its centre and at rest with respect to the DM halo.

These mocks are a subset of the first generation of wide and deep mock galaxy catalogues for the Panoramic Survey Telescope and Rapid Response System (Pan-STARRS) PS1 survey. Further details on their construction are given in Merson et al. (in preparation).

3 PARAMETER OPTIMIZATION USING MOCK CATALOGUES

The minimization or maximization of non-analytic functions that depend on multiple parameters is an intense research area in statistics and computational science. When the dimensionality of the data set is low, typically two–four dimensions, it is straightforward to completely map out the whole parameter space on a grid. However, when the number of parameters is large (e.g. up to eight for our FoF algorithm) then such a computationally intensive approach is not ideal, especially if each set of parameter values requires a series of complex calculations. For our data size and problem considered, each complete grouping takes 10s of seconds, with a full parameter space not necessarily obvious to define. Hence we use the Nelder–Mead optimization technique (i.e. downhill simplex; see Nelder & Mead 1965) that allows for maxima (or minima) to be investigated for non-differentiable functions. The onus is still on the user to choose an appropriate function to maximize. For this work we desire a high group detection rate with a low interloper fraction in each group, and this is the criterion that defines the cost function to be minimized.

3.1 Group cost function

One of the defining characteristics of how we decide to determine grouping quality is that the statistics measured should be two way (bijective). By this we mean that the group catalogue made with this algorithm is an accurate representation on the mock group catalogue, and vice-versa. This is an important distinction since it is possible for the group catalogue to perfectly recover every mock group, but for these to be the minority of the final catalogue, i.e. most of the groups are spurious. This has a serious effect on almost any science goal involving use of the GAMA groups since any given group would be more likely to be false than real – follow-up proposals making use of the groups would be highly inefficient, and any science involving the stacking of detections of multiple groups (X-ray, H I) would be hard to achieve.

With this two-way nature of defining grouping quality in mind, there are two global measures that can be ascertained: how well are the groups and the galaxies within them recovered. To retrieve a group accurately we require the joint galaxy population of the FoF groups and mock haloes to include more than 50 per cent of their respective group members. This is called a bijective match, and it ensures that there is no ambiguity when we associate groups together – it is impossible for a group to bijectively match more than one group. To turn this into a global grouping efficiency statistic we

[3] http://www.g-vo.org/Millennium

[4] FoFHaloes are identified with a linking length of $b = 0.2$ in the underlying DM simulation.

define the following quantities:

$$E_{\rm FoF} = \frac{Ng_{\rm bij}}{Ng_{\rm FoF}}, \tag{9}$$

$$E_{\rm mock} = \frac{Ng_{\rm bij}}{Ng_{\rm mock}}, \tag{10}$$

$$E_{\rm tot} = E_{\rm FoF} E_{\rm mock}, \tag{11}$$

where $Ng_{\rm bij}$, $Ng_{\rm FoF}$ and $Ng_{\rm mock}$ are the number of bijective, FoF and mock groups, respectively. $E_{\rm tot}$ is the global halo finding efficiency measurement (or purity product) we want to use in our maximization statistic, and will be 1 if all groups are bijectively found, and 0 if no groups are determined bijectively.

The second measure of group quality determines how significantly matched individual groups are, in effect it determines the 'purity' of the matching groups. The best two-way matching group is the one which has the largest product for the relative membership fractions between the FoF and mock group. Take for example a FoF group with five members where three of these galaxies are shared with a mock group that has nine members and the other two are shared with a mock group that has three members. In this case the two possible purity products are $3/5 \times 3/9 = 9/45 = 0.2$ and $2/5 \times 2/3 = 4/15 \sim 0.27$, so the latter match would be considered the best quality match. We note in this example that the FoF group is not bijectively matched to any mock group. From the definition of a bijective group above, it is clear that the match quality for a bijective group must always be larger than $1/2 \times 1/2 = 0.25$. Globally we define the following statistics:

$$Q_{\rm FoF} = \frac{\sum_{i=1}^{Ng_{\rm FoF}} P_{\rm FoF}[i]\, Nm_{\rm FoF}[i]}{\sum Nm_{\rm FoF}}, \tag{12}$$

$$Q_{\rm mock} = \frac{\sum_{i=1}^{Ng_{\rm mock}} P_{\rm mock}[i]\, Nm_{\rm mock}[i]}{\sum Nm_{\rm mock}}, \tag{13}$$

$$Q_{\rm tot} = Q_{\rm FoF} Q_{\rm mock}, \tag{14}$$

where $Nm_{\rm FoF}[i]$ and $Nm_{\rm mock}[i]$ are the number of group members in the ith FoF and mock group, respectively. $P_{\rm FoF}[i]$ and $P_{\rm mock}[i]$ are the purity products of the ith best-matching FoF and mock group, respectively. In the example above $P_{\rm FoF} \sim 0.27$ and $Nm_{\rm FoF} = 5$. If a halo is perfectly recovered between the FoF and mock then $P_{\rm FoF}$ and $P_{\rm mock}$ both equal 1 for that matching halo. $Q_{\rm tot}$ is the global grouping purity we want to use in our maximization statistic, and will be 1 if all groups are found perfectly in the FoF catalogue. The lower limit must be more than 0 (since it is always possible to break a catalogue with $N_{\rm gal}$ galaxies into a catalogue of $N_{\rm gal}$ groups), and at worst $Q_{\rm tot} = Ng^2_{\rm mock}/N^2_{\rm gal}$.

Using $E_{\rm tot}$ and $Q_{\rm tot}$ we can now calculate our final summary statistic:

$$S_{\rm tot} = E_{\rm tot} Q_{\rm tot}, \tag{15}$$

where $S_{\rm tot}$ will span the range 0–1.

3.2 Optimization

Whilst it is possible to optimize the set of grouping parameters such that the absolute maximum value for $S_{\rm tot}$ is obtained, in practice some of the parameters barely affect the returned group catalogue as long as sensible values are chosen. For FoF group finding, Δ, r_Δ, l_Δ have a weak affect on the final grouping, and fixing them at 9, $1.5\,h^{-1}$ Mpc and 12 proved to be almost as effective as allowing them to be freely optimized. For expediency they were fixed after this initial determination. The other five FoF parameters do require optimization, the descending order of parameter importance is b_0, R_0, E_b, E_R and ν.

As well as choosing the set of parameters to adjust, the set of groups chosen as the basis of optimization must be considered carefully. The optimization strategy has to be defined depending on the desired goals. Most further studies will make use of the largest and best fidelity groups, and these groups suffer disproportionately if the optimization is carried out using smaller systems and then applied to all of the mock data. Because of this only groups with five or more members were used to determine the appropriate combination of parameters. Part of the justification for this is that five or more members are required to make a meaningful estimate of the dynamical velocity dispersion ($\sigma_{\rm FoF}$) and 50th percentile radius ($\rm Rad_{50-group}$).

To optimize the overall grouping to maximize the output of $S_{\rm tot}$ we used a standard Nelder–Mead (Nelder & Mead 1965) approach, using the OPTIM function available in the R programming environment. We simultaneously attempted to find the optimal combination of the five specified parameters for all nine mock GAMA volumes, a process that took ~ 2 d CPU time. The optimization was done for three different magnitude limits: $r_{\rm AB} \leq 19.0$, ≤ 19.4 and ≤ 19.8 mag. The returned parameters were extremely similar. The set generated for $r_{\rm AB} \leq 19.4$ were the best compromise, producing the highest overall cost for all three depths combines. Since the solutions were so similar, we took the parameters found for $r_{\rm AB} \leq 19.4$ as the single set to be used for all analysis. Table 1 contains the optimal numbers for the five parameters investigated.

The most significant fact to highlight in Table 1 is that E_b and E_R are so close to zero that their effect is completely negligible. Interestingly, if we instead attempt the same optimization problem but remove ν these parameters become more significant, but the final cost for the optimization is not as good. This means the three parameters adapt in a degenerate manner, but the luminosity-based adaptation is the most successful, and the parameter most fundamentally related to optimal galaxy groups. The G³Cv1 will still use all five parameters as specified, but we note that in future extensions to this work E_b and E_R may be removed.

It is clear that the chosen set of parameters produce very similar final $S_{\rm tot}$ for all depths ($\sim$0.4). This implies that on average $E_{\rm FoF}$, $E_{\rm mock}$, $Q_{\rm FoF}$ and $Q_{\rm mock}$ are all $\sim$0.8. Even though no restriction is made in terms of which grouping direction has most significance, the breakdown of each global grouping component indicates that the cost is most easily increased by improving the overall halo finding efficiency, where for $N_{\rm FoF} \geq 5$ (a useful selection since largely groups are typically harder to group accurately), $E_{\rm tot} = 0.69$ and $Q_{\rm tot} = 0.53$. The contribution to the overall cost is also slightly asymmetric from the mock and FoF components: $E_{\rm mock} = 0.89$, $E_{\rm FoF} = 0.77$, $Q_{\rm mock} = 0.73$ and $Q_{\rm FoF} = 0.80$. Overall, the cost of mock groups to $S_{\rm tot}$ is 0.65, and from the FoF groups it is 0.62. These numbers indicate that the FoF algorithm must recover, on average, more groups than actually exist in the mock data. Furthermore, the FoF algorithm is slightly better at constructing the groups it finds than it is at recovering haloes from the data. These statistics mean that the most successful algorithm is necessarily a conservative one where real haloes are robustly and unambiguously detected, and interloper rates kept low in these systems. This is required since it is very easy to create spurious group detections once the grouping is more generous.

Table 1. The optimal global parameters for all groups with $N_{\rm FoF} \geq 5$.

b_0	R_0	E_b	E_R	ν	$S_{\rm tot}(r_{\rm AB} \leq 19.0)$	$S_{\rm tot}(r_{\rm AB} \leq 19.4)$	$S_{\rm tot}(r_{\rm AB} \leq 19.8)$
0.06	18	−0.00	−0.02	0.63	0.40	0.42	0.41

Table 2. The 1σ spread of the optimal grouping parameters found for the nine different mock GAMA lightcones. For the three most important parameters, their relative spread is indicated as well.

σ_{b_0}	σ_{R_0}	σ_{E_b}	σ_{E_R}	σ_ν	σ_{b_0}/b_0	σ_{R_0}/R_0	σ_ν/ν
0.00	1	0.02	0.10	0.06	0.03	0.04	0.09

3.2.1 Parameter sensitivity

To assess how sensitive the best parameters found are to perturbations in the volume investigated (sample variance) we made optimizations for each of the nine GAMA mock volumes. The distribution of the parameters gives us an indication of both how well constrained they are, and how degenerate they are with respect to the other parameters.

A principal component analysis (PCA) of the outcome for five parameters optimized to nine volumes suggests nearly all the parameter variance is explained with just two principal components. The most significant parameters are b and ν, and these are anticorrelated. R is the only other significant parameter that contributes to component 1, and this is anticorrelated closely with b. E_b and E_R dominate the second component, and they are strongly anticorrelated.

Table 2 shows the 1σ spread in optimal parameter values obtained, and gives an indication of how stable our parameters are to the sample selection. The only surprising fact is that E_R is prone to vary quite a large amount depending on the volume, however, this is precisely because it has least influence on the quality of any grouping outcome, and hence a large change can cause minor improvements in the grouping. b is extremely well constrained, which is important to know since it is comfortably the most significant parameter for any FoF grouping algorithm.

4 GROUP PROPERTIES, RELIABILITY AND QUALITY OF GROUPING ALGORITHM

Whilst the primary aim of the grouping algorithm is to maximize the accuracy of the content of the groups, it is essential to derive well-determined global group properties. The group velocity dispersion ($\sigma_{\rm FoF}$) and radius ($r_{\rm FoF}$) are key properties to recover accurately, as they form the most directly inferred group characteristics, together with the group centre and total group luminosity ($L_{\rm FoF}$). The importance of their precise recovery is further strengthened by the expectation that a reasonable dynamical mass estimator is proportional to $\sigma^2_{\rm FoF}$ and $r_{\rm FoF}$ (Section 4.3).

There are many ways to estimate $\sigma_{\rm FoF}$ and $r_{\rm FoF}$, but it is essential for the estimates to be median unbiased and robust to slight perturbations in group membership. Both constraints are important so as to not make our group properties overly sensitive to some precise aspect of the grouping algorithm (a process that will never produce a perfect catalogue).

Hereafter we adopt the following notation. $X_{\rm FoF}$ and $X_{\rm halo}$ correspond to a quantity X measured using galaxies of the FoF mock group and of the underlying/true DM haloes, respectively. The estimate of X is done with the same method both times, i.e. only the galaxy membership changes between the two measurements for matched FoF and halo groups. Matching in the mocks corresponds to the best group matching between FoF groups and intrinsic haloes, defined as the two way match that produces the highest $Q_{\rm tot}$ (see Section 3.1 for further details). We refer to group multiplicity, $N_{\rm FoF}$, as the number of group members a given FoF group has, which has to be distinguished from $N_{\rm halo}$ the true number of group members of a given halo. $X_{\rm mock}$ is a value based on an output of the semi-analytic mock groups directly, it is not measured using a similar method as for the FoF groups. In practice, only the total luminosity of the galaxies in the mock group ($L_{\rm mock}$) require this notation since they are found from summing up the flux of all group members beyond the magnitude limit of the simulated lightcone. Finally, $X_{\rm DM}$ refers to a property that is measured from the Millennium Simulation DM haloes themselves (so not dependent on the semi-analytics in any manner). In practice, only the total mass of all DM particles within the halo ($M_{\rm DM}$) requires this notation.

4.1 Velocity dispersion estimator

The group velocity dispersion, $\sigma_{\rm FoF}$, is measured with the *gapper* estimator introduced by Beers, Flynn & Gebhardt (1990), and used for velocity dispersion estimates in e.g. 2dFGRS Percolation-Inferred Galaxy Group (2PIGG; Eke et al. 2004a). This estimator is unbiased, even for low multiplicity systems, and is robust to weak perturbations in group membership.

In summary, for a group of multiplicity $N = N_{\rm FoF}$, all recession velocities are ordered within the group and gaps between each velocity pair is calculated using $g_i = v_{i+1} - v_i$ for $i = 1, 2\ldots, N - 1$, as well as weights defined by $w_i = i(N - i)$. The velocity dispersion is then estimated via

$$\sigma_{\rm gap} = \frac{\sqrt{\pi}}{N(N-1)} \sum_{i=1}^{N-1} w_i g_i. \tag{16}$$

Based on the fact that in the majority of mock haloes the brightest galaxy is moving with the halo centre of mass, the velocity dispersion is increased by an extra factor of $\sqrt{N/(N-1)}$ (as implemented in Eke et al. 2004a). Equation (16) assumes no uncertainty on the recession velocities, while in reality the accuracy of the redshifts (and therefore recession velocities) depend among other things on the galaxy survey considered. To account for this the velocity dispersion is further modified by the total measurement error $\sigma_{\rm err}$ being removed in quadrature, giving

$$\sigma = \sqrt{\frac{N}{N-1}\sigma^2_{\rm gap} - \sigma^2_{\rm err}}. \tag{17}$$

The total measurement error $\sigma_{\rm err}$ is the result of adding together the expected velocity error for each individual galaxy in quadrature, where we account for the survey origin of the redshift, the leading source of uncertainty in estimating $\sigma_{\rm err}$. The GAMA redshift catalogue is mainly composed of redshifts from GAMA (∼84 per cent), SDSS (∼12 per cent) and 2dFGRS (∼3 per cent) where the typical errors are ∼50, ∼30 and ∼80 km s^{-1} (see Driver et al. 2011, for further details on the redshift uncertainties in the GAMA catalogue).

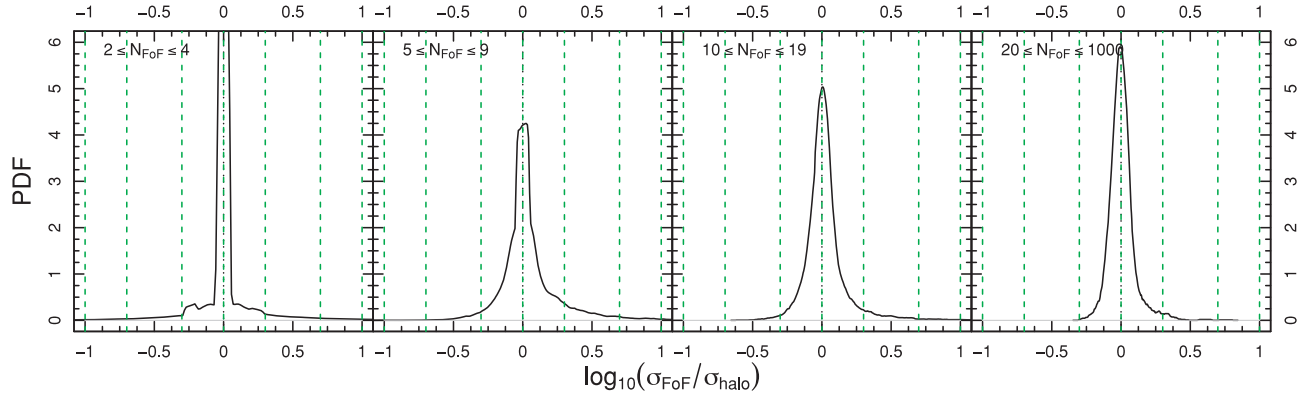

Figure 2. Probability distribution function (PDF) of $\log_{10}\sigma_{\rm FoF}/\sigma_{\rm halo}$, i.e. the log ratio of the measured/recovered velocity dispersion ($\sigma_{\rm FoF}$) to the intrinsic galaxy velocity dispersion ($\sigma_{\rm halo}$), for best-matching FoF/halo mock groups. Each panel shows groups of different multiplicities, as labelled. The vertical dashed lines indicate where $\sigma_{\rm FoF}$ is a factor 2/5/10 off the intrinsic $\sigma_{\rm halo}$. The more peaked and centred on 0 the PDF is, the more accurately the underlying $\sigma_{\rm halo}$ is recovered.

Fig. 2 shows the distribution of the log ratio of the measured/recovered velocity dispersion ($\sigma_{\rm FoF}$) to the intrinsic galaxy velocity dispersion ($\sigma_{\rm halo}$) for best matching FoF/ halo mock groups. Explicitly $\sigma_{\rm halo}$ is estimated using equation (16) with mock GAMA galaxies belonging to the same underlying halo, i.e. $\sigma_{\rm halo}$ does not correspond to the underlying DM halo velocity dispersion. Furthermore, $\sigma_{\rm halo}$ is estimated using only the line-of-sight velocity information. Hence a perfect grouping would result in $\delta_{\rm Dirac}$ distributions in Fig. 2. The fact that these distributions are so tight is a reflection of the quality of the FoF grouping. For ∼80.4 per cent (∼50 per cent) of all mock groups, the recovered $\sigma_{\rm FoF}$ is within ∼50 per cent (∼14 per cent) of the intrinsic value. The distributions are median unbiased for most multiplicities with the mode close to zero as well. The symmetry of Fig. 2 is a good indication that the FoF groups are as likely to underestimate as overestimate the velocity dispersion.

4.2 Group centre and projected radius: definitions and estimators

More contentious quantities to define and estimate are the *centre* and the *projected radius* of a group. First, there is no unique way to define the group centre [e.g. centre of mass (CoM), geometric centre (GC), brightest group/cluster galaxy (BCG), . . .] from which the projected radius is defined. Secondly, the projected radius definition will depend on what fraction of galaxies should be enclosed within it and on what assumption is made for the distance to the group.

To determine the most robust and appropriate definitions for the centre and projected radius of a group a number of schemes were investigated. Hereafter we implicitly assume projected radius when referring to the group radius.

4.2.1 Projected group centre

For the group centre three approaches were considered. First, the group centre was defined as the centre of light (CoL) derived from the $r_{\rm AB}$-band luminosity of all the galaxies associated with the group, which is an easily observable proxy for the CoM. Secondly, an iterative procedure was used where at each step the $r_{\rm AB}$-band CoL was found and the most distant galaxy rejected. When only two galaxies remain, the brighter $r_{\rm AB}$-band galaxy is used as the group centre. We refer to it as Iter. Thirdly, the brightest group/cluster member (BCG) was assumed to be the group centre. For mock groups with $N_{\rm FoF} \geq 5$, 95 per cent of the time the iterative procedure produces the same group centre as the BCG definition.

Fig. 3 presents a comparison between three group centre definitions (Iter, CoL, BCG) and the true/underlying group centre for the best matching (highest $Q_{\rm tot}$) mock groups. In this context 'true' refers to the centre we obtain when running the same algorithm on the exact mock group. The plot shows the distribution of the positional offsets for the different definitions of group centre when compared to the 'truth' for different group multiplicities, with the fraction that agrees perfectly stated in each panel for each group centre definition.

The iterative method always produces the best agreement for the exact group centre and seems to be slightly more robust to the effects of group outliers. As should be expected, the flux weighted CoL definition is the least good at recovering the underlying/true halo centre position. With the CoL definition, the group needs to be recovered exactly to get a perfect match and any small perturbations in membership influences the accuracy with which the centre is recovered. This is very different to the BCG or Iter centre definitions, which are only very mildly influenced by perturbations in membership.

The iterative centre is therefore preferable over merely using the BCG: it has a larger precise matching fraction and a smaller fraction of groups with spuriously large centre offsets. It is very stable as a function of multiplicity, with a fraction of precise group centre matches of ∼90 per cent, as indicated in the panels of Fig. 3. Hereafter we refer to the Iter centre definition as the group centre.

4.2.2 Radial group centre

The group centre definitions as considered in Section 4.2.1 do not necessarily define what the actual group redshift should be. One possible solution is to identify it with the redshift of the central galaxy, as found with the Iter centre definition. An alternative solution would be to select the group redshift as the median redshift of the group members. Fig. 4 presents the distribution of the difference between the recovered median redshift and the intrinsic median redshift for best-matching FoF/halo mock groups. The fraction of group redshifts that agree precisely is stable as a function of multiplicity at ∼55 per cent, and the offset is usually less than 100 km s^{-1}. 80 per cent of the time the redshift differences are within the GAMA

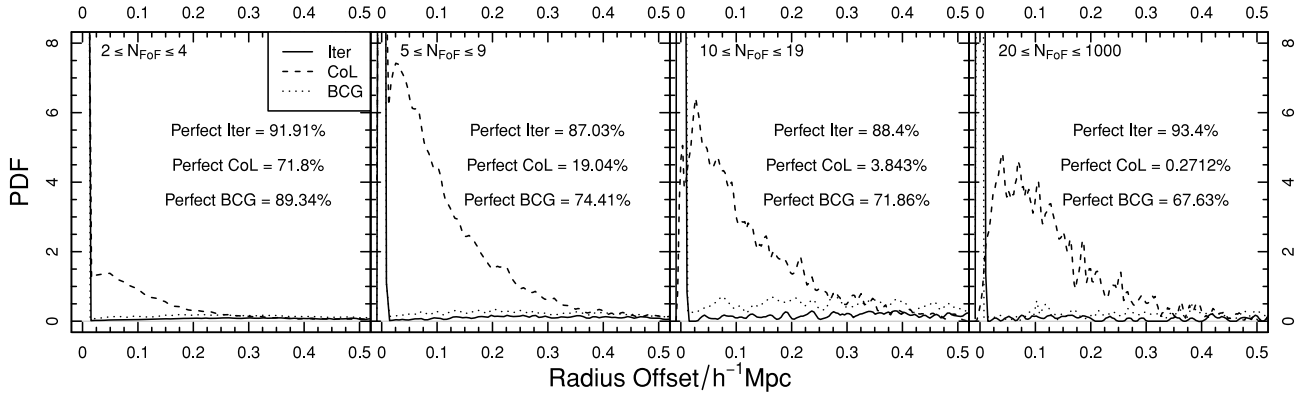

Figure 3. Distribution of position offsets between different group centre definitions and the underlying/true group centre for bijectively matched mock groups. Each panel shows groups of different multiplicities, as labelled. Solid/dashed/dotted lines indicate the Iter/CoL/BCG centre definitions (see text). The nearly vertical lines at small radii correspond to groups which have a perfectly recovered centre position (i.e. zero offset). Their fraction is indicated in the panel as 'Perfect'.

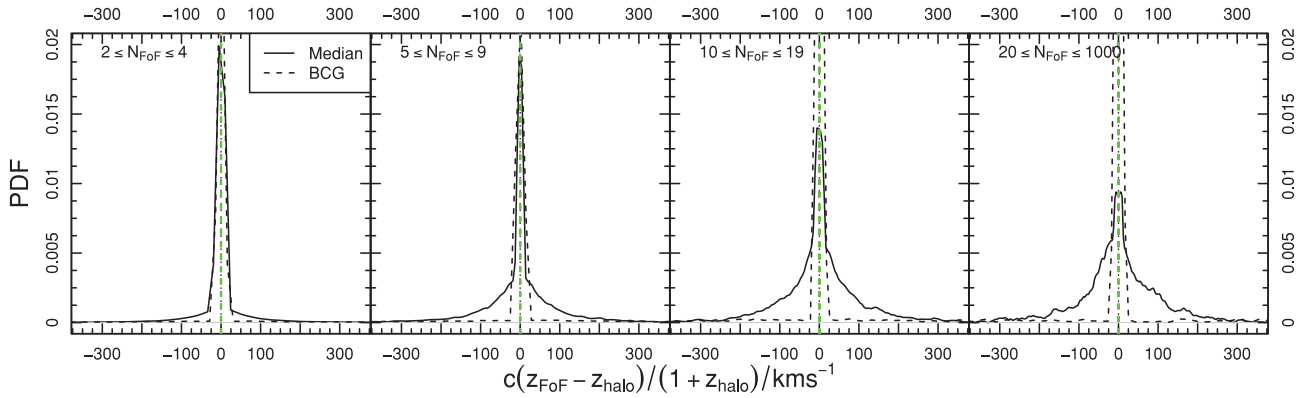

Figure 4. PDF of $z_{\rm FoF} - z_{\rm halo}$ for best-matching FoF/halo mock groups, where z is the median redshift of the group. Each panel shows groups of different multiplicities, as labelled. The fraction of exact matches is indicated in each panel, as 'Perfect'.

velocity error of $\sim$50 km s^{-1} (see Driver et al. 2011, for details). It is essential to notice that this radial centre is defined in redshift space (i.e. including peculiar velocities) as opposed to real space (i.e. based on Hubble flow redshift), as only information for the former is available from a redshift survey. A comparison between the real and the redshift-space centre shows directly the importance and the impact of bulk flow motions, i.e. the galaxy groups themselves are not at rest.

4.2.3 Projected group radius

The radius definition must be a compromise between containing a large enough number of galaxies to be stable statistically and small enough to not be overly biased by or sensitive to outliers and interlopers (which tend to lie at larger projected distances). Three radius definition were considered: $\rm Rad_{50}$, $\rm Rad_{1\sigma}$ and $\rm Rad_{100}$ containing 50, 68 and 100 per cent of the galaxies in the group, respectively. The latter, $\rm Rad_{100}$, is mainly used for illustrative purposes, as it is extremely sensitive to outliers. $\rm Rad_{\it X}$ is defined using the default quantile definition in R, i.e. the group members are sorted in ascending radius value, assigned a specific percentile (the most central 0 per cent and the furthest away 100 per cent) and finally a linear interpolation between the radii of the two relevant percentiles is performed. This implies that only the radial distance of the two galaxies bracketing the percentile definition used are considered in the estimate of $\rm Rad_{\it X}$, explaining why $\rm Rad_{100}$ is expected to be the most sensitive to outliers.

Fig. 5 shows a comparison between three radii definitions as measured from the iterative centre for recovered mock groups ($\rm Rad_{\it X-FoF}$) and for true mock haloes ($\rm Rad_{\it X-halo}$) for best matching FoF/halo mock groups. $\rm Rad_{50}$ is marginally more centrally concentrated than $\rm Rad_{1\sigma}$ for all multiplicity subsets and is hence the least affected by interlopers and outliers.

The subsets plotted in Fig. 5 up to $10 \leq N_{\rm FoF} \leq 19$ are all median unbiased, although there is a slight high-moment excess of large radius groups for $2 \leq N_{\rm FoF} \leq 9$ and a high moment excess of erroneously low-radius groups for $10 \leq N_{\rm FoF} \leq 19$. This does not affect the median of the distribution, but requires the mean to be offset from the median in these cases.

The highest multiplicity subset (rightmost panel of Fig. 5) has an identifiable excess of low-radius groups, leading to a biased median that is $\sim$15 per cent lower than the original aim. Hence the estimated $\rm Rad_{50-FoF}$ for half of the highest multiplicity groups is underestimated by at least $\sim$15 per cent compared to the corresponding underlying $\rm Rad_{50-halo}$. We note however that this definition still behaves better than any of the other two considered.

Whilst the accuracy of the measured velocity dispersion noticeably improves as a function of multiplicity (see Fig. 2), the accuracy of the observed radius does not. This observation should be expected since groups have their centres iterated towards the optimal solution. During this process they, in effect, become lower multiplicity as the

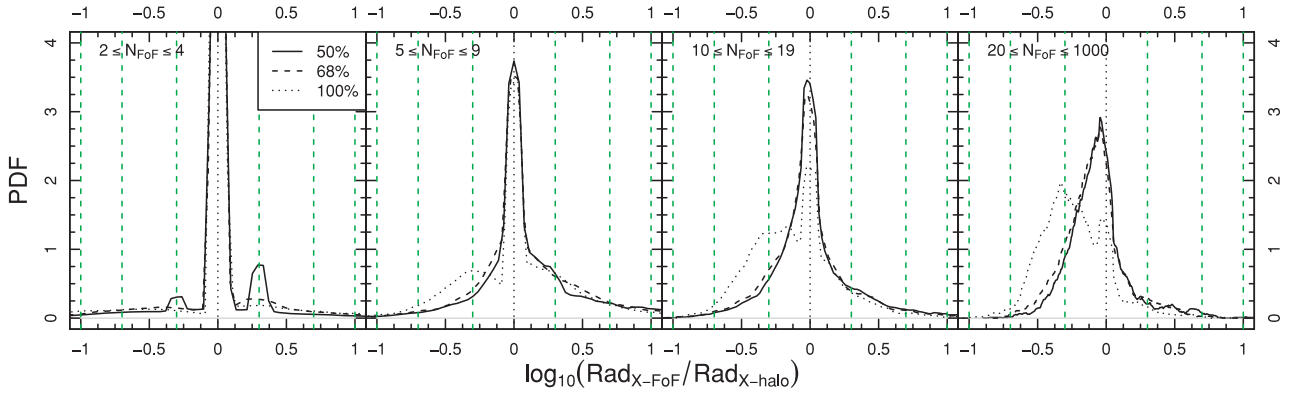

Figure 5. PDF of $\log_{10}$ $\mathrm{Rad}_{X-\mathrm{FoF}}/\mathrm{Rad}_{X-\mathrm{halo}}$, i.e. the log ratio of the measured/recovered radius ($\mathrm{Rad}_{X-\mathrm{FoF}}$) to the intrinsic galaxy radius ($\mathrm{Rad}_{X-\mathrm{halo}}$), for best-matching FoF/halo mock groups. Each panel shows groups of different multiplicities, as labelled. Solid/dashed/dotted lines indicate the Rad_{50}, $\mathrm{Rad}_{1\sigma}$ and Rad_{100} radii definitions, respectively, encompassing 50, 68 and 100 per cent of the galaxies in the group. The solid line, Rad_{50}, produces the tightest distribution of the three considered. The vertical dashed lines indicate where $\mathrm{Rad}_{X-\mathrm{FoF}}$ is a factor of 2/5/10 off the intrinsic $\mathrm{Rad}_{X-\mathrm{halo}}$.

outliers are removed, and thus will suffer from similar numerical artefacts.

Based on the improvement in radius agreement for $N_{\mathrm{FoF}} \geq 5$, Rad_{50} was selected as the preferred definition of radius for use in the G³Cv1. For the remainder of this paper, and in any future discussion of GAMA galaxy groups, any mention of group radius implicitly refers to Rad_{50}. However it is to be noted that $\mathrm{Rad}_{1\sigma}$ is better behaved for low-multiplicity groups ($N_{\mathrm{FoF}} \leq 4$), as the 'bumps' at ± 0.3 in the leftmost panel of Fig. 5 have vanished nearly completely in that case. The origin of these two spikes becomes clear in the discussion of Fig. 6.

4.3 Dynamical group mass estimator and calibration

Once an unbiased and robust group velocity dispersion and a nearly unbiased group radius can be estimated, the final step is to combine this information into a dynamical mass estimator. To first order for a virialized system we expect its dynamical mass to scale as $M \propto \sigma^2 R$, where σ and R are calculated as described in Sections 4.1 and 4.2.

To understand any correlated biases in the estimates of these two fundamental group properties, we plot in Fig. 6 the group density distribution as a function of the relative accuracy of the recovered group radius (x-axis) and the square of the group velocity dispersion (y-axis). More precisely Fig. 6 shows the group density distribution

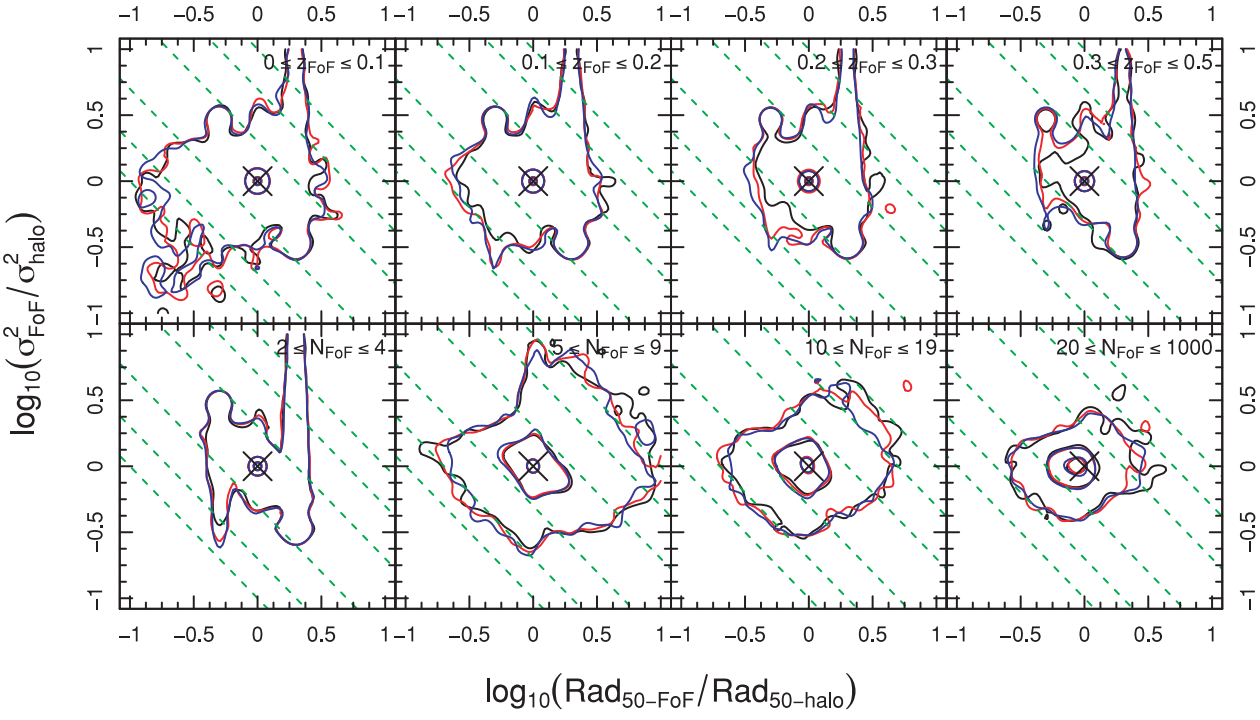

Figure 6. 2D density distribution of the best-matching FoF/halo mock groups in the $\log_{10}$ $\mathrm{Rad}_{X-\mathrm{FoF}}/\mathrm{Rad}_{X-\mathrm{halo}}$–$\log_{10}(\sigma_{\mathrm{FoF}}/\sigma_{\mathrm{halo}})^2$ plane, split as a function of redshift and multiplicity (top and bottom panel, respectively). The x and y-axes show the relative accuracy of the recovered radius and velocity dispersion (squared), respectively. The contours represent the regions containing 10/50/90 per cent of the data for three magnitude limits, i.e. $r_{\mathrm{AB}} \leq 19.0$ (black), $r_{\mathrm{AB}} \leq 19.4$ (red) and $r_{\mathrm{AB}} \leq 19.8$ (blue). The green dashed lines delineate regions where $\sigma^2_{\mathrm{FoF}}\mathrm{Rad}_{50-\mathrm{FoF}}$ is 2/5/10 times off the expectation given by $\sigma^2_{\mathrm{halo}}\mathrm{Rad}_{50-\mathrm{halo}}$, reflecting to some extent the implied uncertainty on any dynamical mass estimate (see text for details).

in the $\log_{10}\mathrm{Rad_{X\text{-}FoF}}/\mathrm{Rad_{X\text{-}halo}}-\log_{10}(\sigma_{\mathrm{FoF}}/\sigma_{\mathrm{halo}})^2$ plane, split as function of redshift and multiplicity, with ranges specified in each panel. The green dashed lines delineate regions where $\sigma^2_{\mathrm{FoF}}\mathrm{Rad_{50\text{-}FoF}}$ is 2/5/10 times off the expectation given by $\sigma^2_{\mathrm{halo}}\mathrm{Rad_{50\text{-}halo}}$, reflecting to some extent the implied uncertainty on any dynamical mass estimate. As a matter of fact, if the dynamical mass is proportional to $\sigma^2 R$ as expected for a virialized system and can be directly estimated from $\sigma^2_{\mathrm{halo}}\mathrm{Rad_{50\text{-}halo}}$, then the green dashed lines indicate by what amount the halo mass as inferred from $\sigma^2_{\mathrm{FoF}}\mathrm{Rad_{50\text{-}FoF}}$ deviates from the true one (assuming the same proportionality factor). Additionally any asymmetry in the density distribution with respect to those guide lines is a sign of a bias in the inferred mass: a density excess in the top-right/bottom-left of any panel indicates a bias towards incorrectly high/low dynamical masses. Note that a density excess orthogonal to these lines is not problematic for the mass estimates since the individual biases cancel out in this parametrization.

As a function of redshift the density distributions in Fig. 6 are well behaved. As a function of multiplicity the main effect is a tightening of the distribution, which is expected since the velocity dispersion and, to a lesser degree, the radius can be better estimated with more galaxies. The $5 \leq N_{\mathrm{FoF}} \leq 9$ multiplicity range shows some small bias towards high dynamical masses (the 90 per cent contour wing) whilst the highest multiplicity subset ($20 \leq N_{\mathrm{FoF}} \leq 1000$) appears to be biased to slightly low dynamical masses (offset for 10 and 50 per cent contour wings). Overall the biases are small for $N_{\mathrm{FoF}} \geq 5$ multiplicity groups, and in the tails of the distributions rather than in the median or the mode. However, for low-multiplicity groups ($N_{\mathrm{FoF}} \leq 4$) the situation is rather different. First of all, there is an extensive scatter in the recovered velocity dispersion at $\log_{10}\mathrm{Rad}_{X-\mathrm{FoF}}/\mathrm{Rad}_{X-\mathrm{halo}} \simeq \pm 0.3$. This is entirely related to the 'bumps' seen in Fig. 5 and is due to mismatches in the grouping, explaining why the velocity dispersions are so poorly recovered for some of those systems. The reason for an overdensity of groups at ± 0.3 (i.e. half/double the underlying radius) is related to the way $\mathrm{Rad_{50}}$ works. When a $N_{\mathrm{FoF}} = 2$ group misses one member and when a $N_{\mathrm{FoF}} = 3$ group contains one interloper this results most often in a FoF group where the calculated group centre is the same[5] but radius that is half and double the halo radius, respectively. Additionally any asymmetry seen in the top panels of Fig. 6 can be attributed to low-multiplicity groups. Generally Fig. 6 gives us confidence that measurement errors in σ^2 and R are not highly correlated.

The dynamical mass of a system is estimated using

$$\frac{M_{\mathrm{FoF}}}{h^{-1}\,\mathrm{M}_\odot} = \frac{A}{G/(\mathrm{M}_\odot{}^{-1}\mathrm{km^2\,s^{-2}Mpc})}\left(\frac{\sigma_{\mathrm{FoF}}}{\mathrm{km\,s^{-1}}}\right)^2 \frac{\mathrm{Rad_{FoF}}}{h^{-1}\,\mathrm{Mpc}}, \quad (18)$$

where G is the gravitational constant in suitable units, i.e. $G = 4.301 \times 10^{-9}\,\mathrm{M}_\odot{}^{-1}\mathrm{km^2\,s^{-2}Mpc}$. A is the scaling factor required to create a median unbiased mass estimate of $M_{\mathrm{DM}}/M_{\mathrm{FoF}}$. For a 'typical' cluster with a $1\,h^{-1}$ Mpc radius and a velocity dispersion of $1000\,\mathrm{km\,s^{-1}}$, the mass given by equation (18) is $\sim 2A \times 10^{14}\,h^{-1}\,\mathrm{M}_\odot$. A is likely to be larger than unity, since the estimated velocity dispersion using equation (16) traces the velocity dispersion along the line of sight only[6] and the average projected radius is smaller than the average intrinsic radius.[7] Finally, equation (18) can only be truly valid for a system in virial equilibrium, which many of our system will not necessarily be. Hence the best approach is to determine A in a semi-empirical manner by requiring it to produce a median unbiased halo mass estimate when comparing best matching FoF/halo mock groups.

Performing a single global optimization using all bijectively matched groups with $N_{\mathrm{FoF}} \geq 5$ results in $A = 10.0$. This is somewhat different to this $A = 5$ factor found in Eke et al. (2004a). This should not be surprising since there are differences in the style of grouping optimization, and we have used a more compact definition of the group radius and a different approach to recovering the group centre. It is interesting to note that this scaling of $A = 10.0$ is identical to the dynamical mass scaling found in Chilingarian & Mamon (2008) for calculating the virial mass of dwarf galaxies.

Fig. 7 compares the median globally calibrated dynamical masses to the underlying DM halo mass for best matching FoF/halo mock groups (using $A = 10.0$). Whilst the distribution is globally unbiased for $N_{\mathrm{FoF}} \geq 5$ (by definition), small deviations as a function of redshift and/or multiplicity are evident. Offsets from the median line are evident at all multiplicities, but strongest for low-multiplicity systems (i.e. $2 \leq N_{\mathrm{FoF}} \leq 4$ groups in Fig. 7). The small biases become more apparent at higher redshifts, driven by the average observed group multiplicity dropping as a function of redshifts and the average mass increasing. To gauge how sensitive the scaling factor A is to the specific subset of data considered combined cuts in redshift and multiplicity were made. Table 3 contains the various A factors required for the different subsets as a function of the possible limiting magnitudes for the GAMA group catalogue.

Using the data in Table 3 the best-fitting plane that accounts for the variation of A as a function of $\sqrt{N_{\mathrm{FoF}}}$ and $\sqrt{z_{\mathrm{FoF}}}$ is calculated. To prevent strong biases to low N_{FoF} systems purely by virtue of their overwhelming numbers, the plane was not weighted by frequency and should produce the appropriate corrections throughout the parameter space investigated. The plane function for A is given by

$$A(N_{\mathrm{FoF}}, z_{\mathrm{FoF}}) = A_c + \frac{A_N}{\sqrt{N_{\mathrm{FoF}}}} + \frac{A_z}{\sqrt{z_{\mathrm{FoF}}}}, \quad (19)$$

where A_c, A_N and A_z are constants to be fitted. Table 4 contains the parameters that produce the best-fitting planes for the three different GAMA magnitude limits. The motivation for the functional form is mainly driven to ensure positivity of $A(N_{\mathrm{FoF}}, z_{\mathrm{FoF}})$ over the range of GAMA multiplicities and redshifts, and a good fit to the data within these limits. The errors shown in Table 4 are estimated from finding the best-fitting plane for the nine mock GAMA volumes separately and measuring the standard deviation of the individual best-fitting planes, much like the approach used for Table 2.

4.3.1 Mass estimate scatter

It is important to highlight that even though the observed dynamical mass estimates and halo masses are well correlated (in particular the scatter is approximately mirrored across the 1–1 line in Fig. 7), it is impossible to select an unbiased subset of mass unless the selection is across the mode of the distribution. This is due to Eddington bias rather than any intrinsic issue with the mass estimates – since most haloes in GAMA will have moderate masses ($\sim 10^{13}\,h^{-1}\,\mathrm{M}_\odot$) if simple Gaussian scatter in mass estimates is assumed, then a high-mass subset must contain a larger fraction of lower mass haloes scattered *up* in mass, and a low-mass subset must contain a larger fraction of higher mass haloes scattered *down* in mass, hence the medians are biased. This effect is different to a Malmquist bias,

[5] Because the group centre is so accurately recovered, see Fig. 3.

[6] For isotropic systems $\sigma_{3\mathrm{D}} \sim \sqrt{3}\sigma_{1\mathrm{D}}$.

[7] For isotropic systems the relation depends on the exact radius definition. Conceptually the 3D and 2D radius will agree for $\mathrm{Rad_{100}}$ but increasingly disagree as the radius measured becomes smaller due to the relative concentration of objects towards the centre when observing a projected 2D, as opposed to intrinsic 3D, distribution.

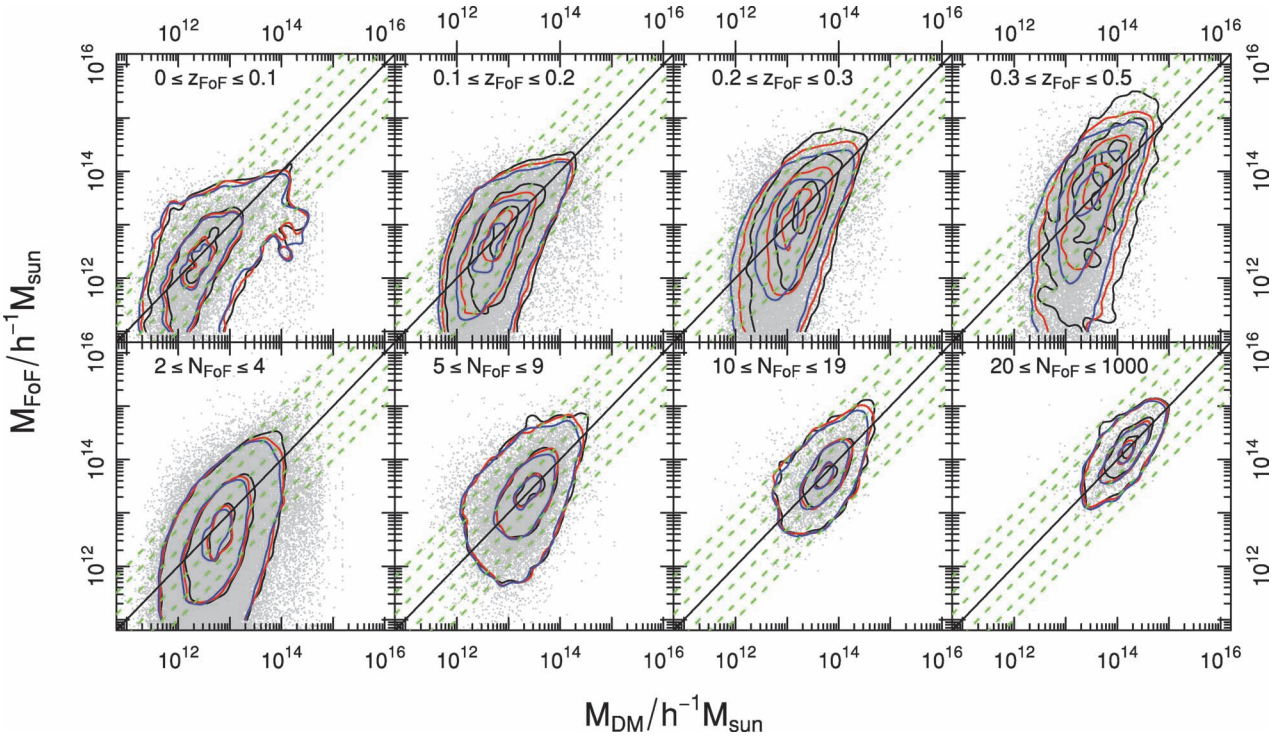

Figure 7. 2D density distribution of best-matching FoF/halo mock groups in the $M_{\rm FoF}$–$M_{\rm DM}$ plane, split as a function of redshift and multiplicity (top and bottom panel, respectively). These panels objectively compare the recovered group masses to the underlying DM halo masses. The contours represent the regions containing 10/50/90 per cent of the data for three magnitude limits, i.e. $r_{\rm AB} \leq 19.0$ (black), $r_{\rm AB} \leq 19.4$ (red) and $r_{\rm AB} \leq 19.8$ (blue). The dots indicate the exact $M_{\rm FoF}$–$M_{\rm DM}$ pairs. For $M_{\rm FoF}$ we use equation (18) and $A = 10.0$. The green dashed lines delineate regions where $M_{\rm FoF}$ is 2/5/10 times off the underlying $M_{\rm DM}$.

Table 3. Values of A, the dynamical mass scaling factor of equation (18), required to create an unbiased median mass estimate for different disjoint subsets of bijectively matched groups.

	$2 \leq N_{\rm FoF} \leq 4$			$5 \leq N_{\rm FoF} \leq 9$			$10 \leq N_{\rm FoF} \leq 19$			$20 \leq N_{\rm FoF} \leq 1000$		
	19.0	19.4	19.8	19.0	19.4	19.8	19.0	19.4	19.8	19.0	19.4	19.8
$0 \leq z_{\rm FoF} \leq 0.1$	20.0	19.0	18.0	11.8	10.8	10.9	11.4	12.0	11.5	12.1	12.6	12.7
$0.1 \leq z_{\rm FoF} \leq 0.2$	20.2	19.5	19.2	10.3	10.5	10.7	11.0	11.1	10.9	9.2	10.4	10.9
$0.2 \leq z_{\rm FoF} \leq 0.3$	21.2	21.5	19.8	9.0	10.3	11.2	8.0	8.6	9.9	6.7	8.3	9.6
$0.3 \leq z_{\rm FoF} \leq 0.5$	13.6	17.4	17.8	4.4	6.1	7.9	3.5	5.4	6.7	4.8	5.6	6.9

which explains the observational bias in distribution of halo masses as a function of distance.

This effect can be modelled quite accurately by assuming we have median unbiased lognormal relative error in the mass estimate, where the standard deviation of the distribution ($M_{\rm err}$) is a function of system multiplicity. The effect multiplicity has on the accuracy of the mass can be seen clearly in Fig. 8, where although median unbiased for $N_{\rm FoF} \geq 4$, the standard deviation of the distribution decreases strongly as a function of multiplicity. The approximate function for this effect is given by

$$\log_{10}\left(\frac{M_{\rm err}}{h^{-1}\,{\rm M}_\odot}\right) = 1.0 - 0.43\log_{10}(N_{\rm FoF}), \quad (20)$$

where the appropriate range of use is $2 \leq N_{\rm FoF} \leq 50$, beyond which the standard deviation is ∼0.27. We recast this error function back on to the intrinsic mock halo masses to give a new mass with simulated dynamical mass errors:

$$\frac{M_{\rm sim}}{h^{-1}\,{\rm M}_\odot} = \frac{M_{\rm DM}}{h^{-1}\,{\rm M}_\odot}\,10^{G(0,\log_{10}(M_{\rm err}/h^{-1}\,{\rm M}_\odot))}, \quad (21)$$

Table 4. List of parameters that create the best-fitting plane to the data in Table 3. The plane is a function of group redshift and multiplicity, as given in equation (19). Errors are estimated from running plane fits to the nine mock GAMA volumes separately and measuring the standard deviation of the individual best-fitting planes.

	A_c	A_N	A_z
$r_{\rm AB} \leq 19.0$	-4.3 ± 3.1	22.5 ± 1.7	3.1 ± 1.1
$r_{\rm AB} \leq 19.4$	-1.2 ± 1.7	20.7 ± 1.4	2.3 ± 0.6
$r_{\rm AB} \leq 19.8$	$+2.0 \pm 1.4$	17.9 ± 1.1	1.5 ± 0.4

where $G(\bar{x}, \mu)$ is a random sample from the normal distribution with a mean $\bar{x}$ and standard deviation μ. Fig. 9 shows how the intrinsic halo mass compares for the same halo masses but with our fiducial error function applied. This shows the main contour twisting features described above – particular clear is the sampling bias you would expect when selecting groups based on the *observed* halo

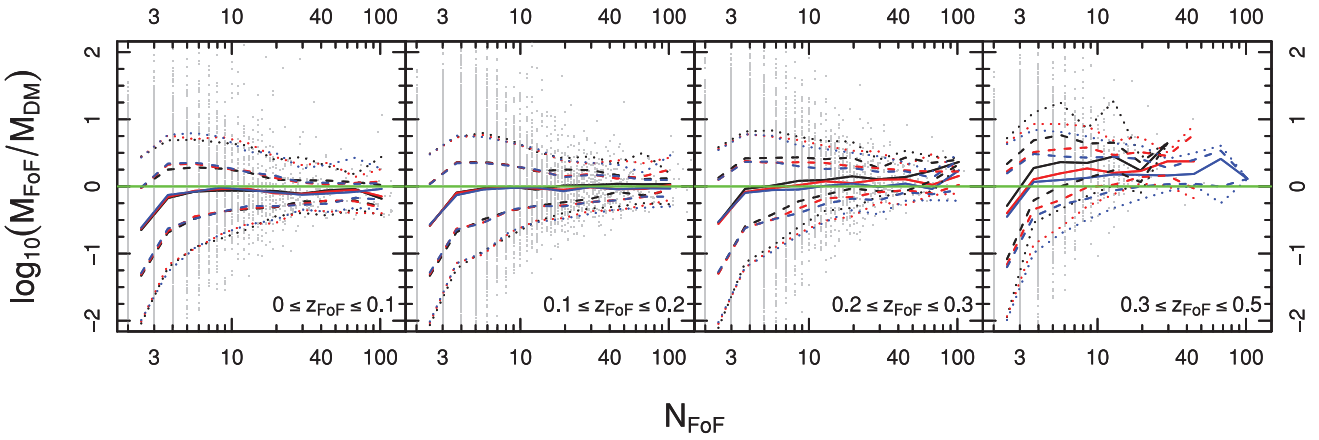

Figure 8. Relative difference between measured and underlying group masses as a function of multiplicity for different redshift subsets. The improvement in the measurement of the velocity dispersion and the radius tightens the distribution until $N_{\rm FoF} \sim 50$. The lines represent the three survey depths of interest: $r_{\rm AB} \leq 19.0$ (black) $r_{\rm AB} \leq 19.4$ (red) and $r_{\rm AB} \leq 19.8$ (blue). For $M_{\rm FoF}$ we use equation (18) and $A = 10.0$.

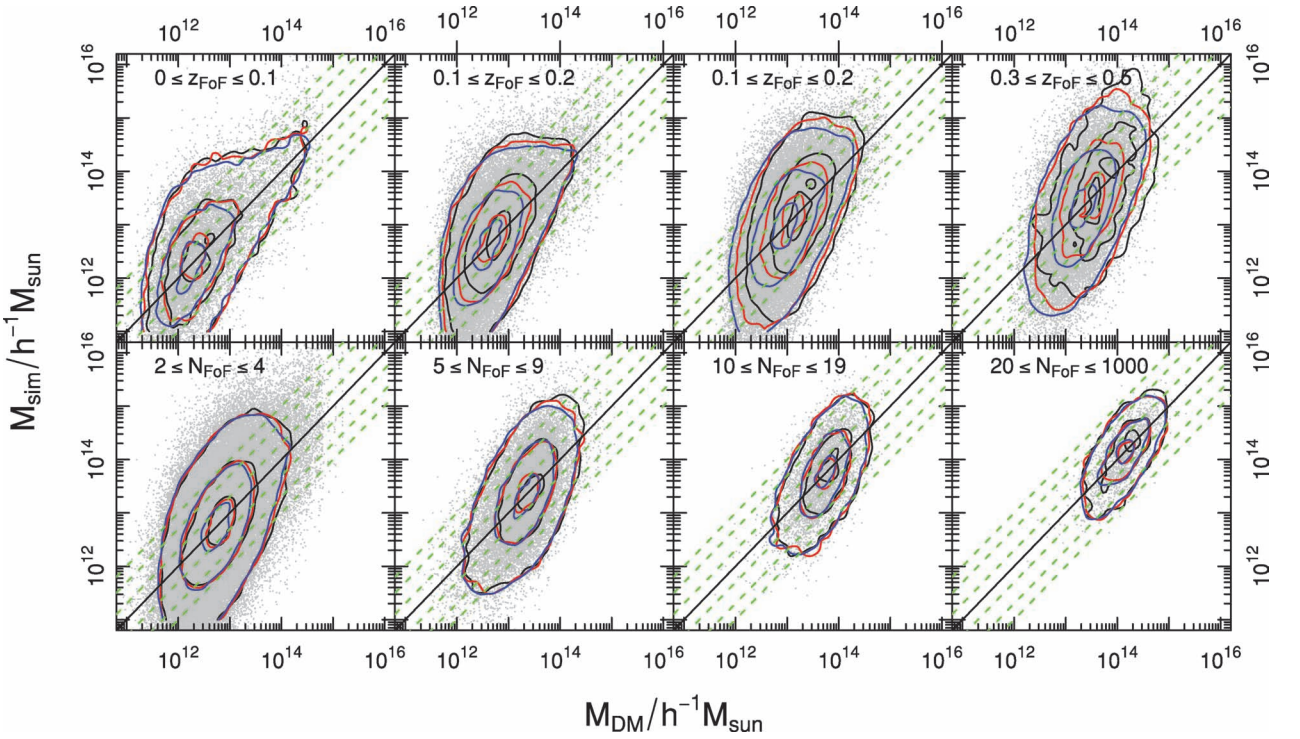

Figure 9. As Fig. 7, but for the simulated relation between $M_{\rm DM}$ and $M_{\rm sim}$ ($M_{\rm DM}$ with the expected random errors applies using equation 21), by modelling the expected error just as a function of group multiplicity. The contours represent the regions containing 10/50/90 per cent of the data for three different magnitude limits: $r_{\rm AB} \leq 19.0$ (black), $r_{\rm AB} \leq 19.4$ (red) and $r_{\rm AB} \leq 19.8$ (blue). $M_{\rm sim}$ is estimated using equation (20).

masses. For instance, the manner in which the mode of the contours appears to be more vertical than the 1–1 line in Fig. 7 (the slight rotation of the contours) is well replicated in Fig. 9 and can be explained by the random scatter of the measured dynamical mass from the intrinsic halo mass.

4.4 Total group luminosity estimator

The total group luminosity is an equally important global group property. It should not be just the total luminosity of the observed group members but the total luminosity as inferred from an arbitrarily faint absolute magnitude limit cut in order to address residual selection effects. To do this we calculate the effective absolute magnitude limit of each group, measure the $r_{\rm AB}$-band luminosity contained within this limit and then integrate the global GAMA galaxy LF (see Section 2.2) to a nominal faint limit used to correct for the missing flux. Explicitly, for each group we calculate the following:

$$L_{\rm FoF} = B\, L_{\rm ob}\, \frac{\int_{-30}^{-14} 10^{-0.4 M_r} \phi_{\rm GAMA}(M_r)\, {\rm d}M_r}{\int_{-30}^{M_{r-{\rm lim}}} 10^{-0.4 M_r} \phi_{\rm GAMA}(M_r)\, {\rm d}M_r}, \quad (22)$$

where $L_{\rm ob}$ is the total observed $r_{\rm AB}$-band luminosity of the group, B is the scaling factor required to produce a perfectly median unbiased

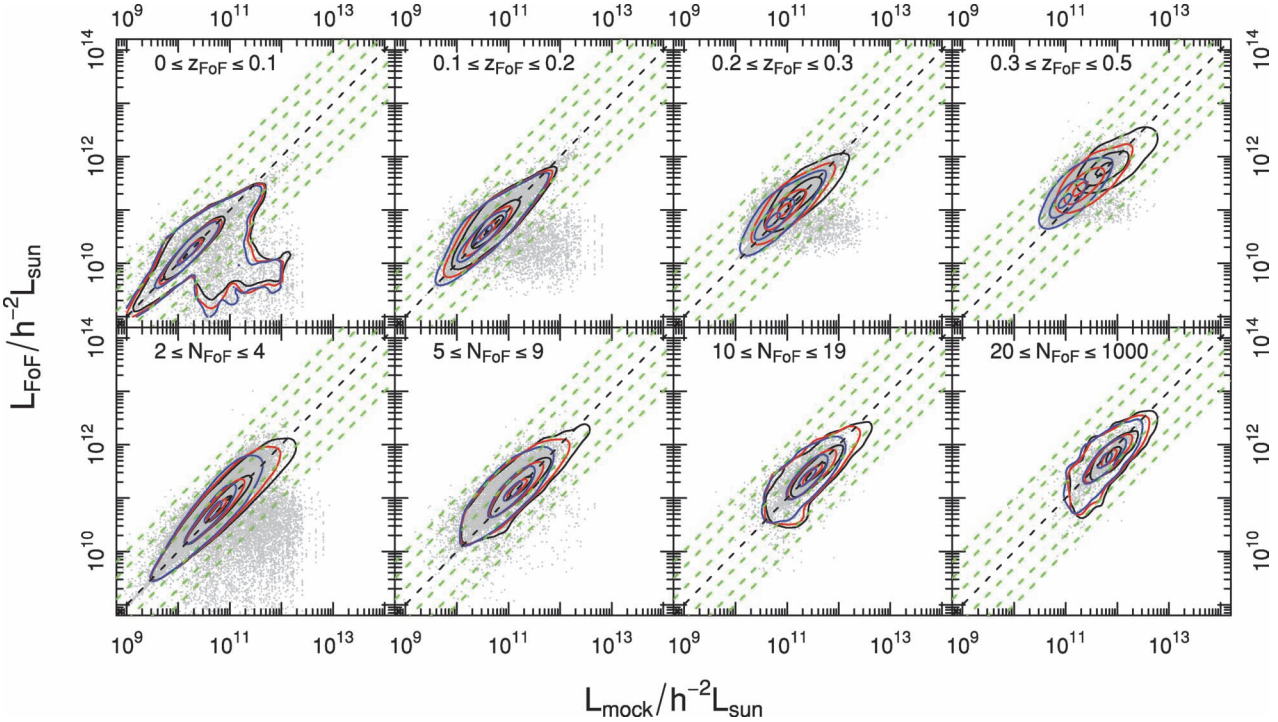

Figure 10. 2D density distribution of best-matching FoF/halo mock groups in the $L_{\rm FoF}$–$L_{\rm mock}$ plane, split as a function of redshift and multiplicity (top and bottom panel, respectively). These panels objectively compare the recovered group luminosities to the underlying total luminosity in the mocks. The contours represent the regions containing 10/50/90 per cent of the data for three magnitude limits, i.e. $r_{\rm AB} \leq 19.0$ (black), $r_{\rm AB} \leq 19.4$ (red) and $r_{\rm AB} \leq 19.8$ (blue). The dots indicate the exact $L_{\rm FoF}$–$L_{\rm mock}$ pairs. The green dashed lines delineate regions where $L_{\rm FoF}$ is 2/5/10 times off the underlying $L_{\rm mock}$. For $L_{\rm FoF}$ we use equation (22) and $B = 1.04$.

luminosity estimate and $M_{r-\rm lim}$ is the effective $r_{\rm AB}$-band absolute magnitude limit for the group. This limit depends on the redshift of observation and apparent magnitude limit used. Corrections are only a few per cent at low redshift when using $r_{\rm AB} \leq 19.8$ and can become factors of a few at $z_{\rm FoF} \sim 0.5$. To convert magnitudes into solar luminosities we take the $r_{\rm AB}$-band absolute magnitude of the Sun to be $M_{r\odot} = 4.67$.[8] The limits of $-30 \leq M_r \leq -14$ used in the numerator of equation (22) are effective limits of $-\infty \leq M_r \leq \infty$ since the luminosity density of a typical LF is nearly all recovered within a couple of magnitudes of M^*. Assuming the Schechter function parameters of Blanton et al. (2003) we would expect to retrieve 99.5 per cent of the intrinsic flux using these limits, assuming the LF continues down to infinitely faint galaxies. More practically, the bright limit ($M_r \geq -30$) is much brighter than any known galaxy, and the faint limit ($M_r \leq -14$) is the limit of the GAMA SWML LF used for this work, and thus is also the effective limit of the mock catalogues used since the galaxy luminosities were adjusted to return the GAMA LF.

Since the median redshift of GAMA is $z \sim 0.2$ and the apparent magnitude limit is at least $r_{\rm AB} = 19.4$, most groups will contain members faintwards of M_h^* (with $M_h^* = M^* - 5\log_{10}h = -20.44$; Blanton et al. 2003). Because the luminosity density is dominated by galaxies around M_h^*, the extrapolation required to get a total group luminosity will be quite conservative since most groups are sampled well beyond M_h^*.

This process assumes that a global LF is appropriate for all groups over a range of masses and environments, which is known not to be the case (e.g. Eke et al. 2004b; Croton et al. 2005; Robotham et al. 2006). However, since the median luminosity scaling is less than a factor of 1.6, the difference that adjusting to halo specific LFs would have to the integrated light will usually be smaller than the statistical scatter observed (which is many 10s of per cent).

Performing a single global optimization using all bijectively matched groups with $N_{\rm FoF} \geq 5$ results in $B = 1.04$. This number accounts for a number of competing effects: the shape of the faint-end slope (α) and the characteristic magnitude (M^*) varying between grouped environments and the global average, and the effects of interloper flux biasing the extrapolated group luminosities. Overall the effects are rather small, and globally we see a value close to 1, which implies neither a large amount of undergrouping nor overgrouping.

Fig. 10 compares the inferred total group luminosity ($L_{\rm FoF}$) to the underlying mock luminosity ($L_{\rm mock}$) for best-matching FoF/mock galaxy groups. The typical scatter as a function of mock group luminosity is quite constant regardless of group multiplicity, with only an excessive amount of scatter for the lowest multiplicity groups, as evidenced in the bottom left-hand panel of Fig. 10. The relations are mostly unbiased, except for the two higher redshift samples (top right-hand panels of Fig. 10).

The scatter in extrapolated group luminosity is much smaller than seen for dynamical masses in Fig. 7. This is expected since fewer observables are required in its estimate and the effect of interlopers is much smaller. By their nature, interlopers are more likely to systematically affect 'geometrical' quantities, like biasing the observed velocity dispersion and radius, while having a lesser impact on e.g. total luminosities. This is because the nature of the optimal grouping used for this work means that on average we should miss as many true group galaxies as add interlopers, so the net loss and gain of galaxy luminosities tend to balance out.

[8] http://mips.as.arizona.edu/~cnaw/sun.html

Table 5. Values of B, the luminosity scaling factor of equation (22), required to create an unbiased median halo luminosity estimate for different disjoint subsets of bijectively matched groups.

	$2 \leq N_{\rm FoF} \leq 4$			$5 \leq N_{\rm FoF} \leq 9$			$10 \leq N_{\rm FoF} \leq 19$			$20 \leq N_{\rm FoF} \leq 1000$		
	19.0	19.4	19.8	19.0	19.4	19.8	19.0	19.4	19.8	19.0	19.4	19.8
$0 \leq z_{\rm FoF} \leq 0.1$	1.1	1.1	1.1	1.1	1.1	1.1	1.4	1.3	1.2	1.8	1.7	1.6
$0.1 \leq z_{\rm FoF} \leq 0.2$	1.0	1.0	1.0	1.1	1.0	1.0	1.2	1.1	1.1	1.3	1.2	1.2
$0.2 \leq z_{\rm FoF} \leq 0.3$	1.0	0.9	0.9	1.1	1.0	0.9	1.2	1.0	1.0	1.2	1.1	1.0
$0.3 \leq z_{\rm FoF} \leq 0.5$	1.1	0.8	0.7	1.2	0.9	0.7	1.5	1.0	0.8	1.1	1.2	0.9

Table 6. List of parameters that create the best-fitting plane to the data in Table 5. The plane is a function of group redshift and multiplicity, as given in equation (22). Errors are estimated from running plane fits to the nine mock GAMA volumes separately and measuring the standard deviation of the individual best-fitting planes.

	B_c	B_N	B_z
$r_{\rm AB} \leq 19.0$	$+1.27 \pm 0.38$	-0.67 ± 0.25	0.08 ± 0.10
$r_{\rm AB} \leq 19.4$	$+0.94 \pm 0.12$	-0.67 ± 0.11	0.16 ± 0.04
$r_{\rm AB} \leq 19.8$	$+0.65 \pm 0.06$	-0.50 ± 0.06	0.22 ± 0.02

As with the dynamical mass estimates, scaling factors, listed in Table 5, are calculated for various redshift and multiplicity subsets in order to properly quantify outstanding biases that remain after scaling the observed luminosities to account for galaxies below the survey flux limit. They are distributed around unity, which is what we would expect if the extrapolated flux fully accounts for all of the missing flux. The variation in the median seen in the table is larger than seen for the dynamical mass scaling factors. This is because we have applied a global LF correction to the data and the LF is known to vary strongly as a function of group environment (e.g. Robotham et al. 2006). Since we are naturally more sensitive to higher mass groups at higher redshifts, this explains the strong redshift gradient scaling factor required, and in comparison the multiplicity variation is very small. For the dynamical A factors the dominant variable was the group multiplicity. When using the groups this is an important consideration: the group dynamical masses are more intrinsically stable (require smaller corrections) as a function of redshift, whilst group luminosities are more stable as a function of multiplicity.

As with the dynamical masses, the total group luminosity correction factors (B) can be well described by a plane that fits Table 5 viz.:

$$B(N_{\rm FoF}, z_{\rm FoF}) = B_c + \frac{B_N}{\sqrt{N_{\rm FoF}}} + \frac{B_z}{\sqrt{z_{\rm FoF}}}, \quad (23)$$

where B_c, B_N and B_z are constants to be fitted. Table 6 contains the best parameters that produce the best-fitting planes for the three different GAMA magnitude limits. The errors shown in Table 6 are estimated from finding the best-fitting plane for the nine mock GAMA volumes separately and measuring the standard deviation of the individual best-fitting planes, much like the approach used for Table 2.

4.5 Group mass and light

The M/L observed in groups is a fundamental property of interest in the analysis of galaxy groups. It is obviously important that any intrinsic scatter in the estimates of both mass and luminosity of groups is not strongly correlated.

Fig. 11 shows the observed fidelity of the group dynamical masses compared to the total group luminosities for a variety of data subsets. Encouragingly the dynamical mass and luminosity estimates do not correlate strongly in any direction – the most significant concern would be strong scatter along the -45° direction since this would mean that the dynamical mass estimates tend to be erroneously small when the luminosity estimates tend to be erroneously large (creating a very small M/L ratio) and vice-versa. Instead the two group measurements show no strong correlations in the accuracy of their recovery.

To demonstrate the improvement witnessed when using the multiplicity and redshift scaling relations, Fig. 12 compares side by side the scatter expected for a simple median correction for $N_{\rm FoF} \geq 5$ (left-hand panel) and for a redshift- and multiplicity-dependent correction (right-hand panel). The dynamical mass and luminosity scaling corrections use equations (19) and (23) with parameters listed in Tables 4 and 6, respectively. The scatter in the recovered luminosity is significantly reduced in the right-hand panel.

It is clear that using the full multiparameter scaling relations offers an improved distribution of mass and luminosity scatter, as well as creating extremely unbiased medians for the distributions. The three apparent magnitude limits used are brought into closer alignment after applying the correction, and the amount of scatter is reduced. The most significant change is for the 90 per cent contour for high $L_{\rm FoF}/L_{\rm mock}$, where we see the contours tighten into very close agreement once the correction is made. This means that groups extracted from regions of different depths (e.g. G09 and G15 versus G12) can be compared more directly. It is also clear that the mode and median are brought into better agreement, moving up towards $L_{\rm FoF}/L_{\rm mock} = 1$.

Depending on the precise science goal the full scaling equations should be used. Particular cases would be in any comparison of extremely dissimilar groups over a large redshift baseline. However, in small volume-limited samples a simple median correction factor might be desirable. This is particularly true at small redshift where the asymptotic nature of the plane function used could produce spurious results.

4.6 Quality of grouping

The accuracy with which the galaxy composition of a group is recovered is a distinct issue, but nevertheless equally important as the precise recovery of intrinsic group properties, as considered in Sections 4.1–4.4. For instance, even a group that has been perfectly recovered might produce an incorrect mass estimate, the latter depending on the exact observed configuration of galaxies on the sky and not solely on the group membership. Using $Q_{\rm tot}$, as defined by equation (14) in Section 3.1, as our definition of grouping quality, we can investigate how different aspects of grouping affect the purity of the observed systems.

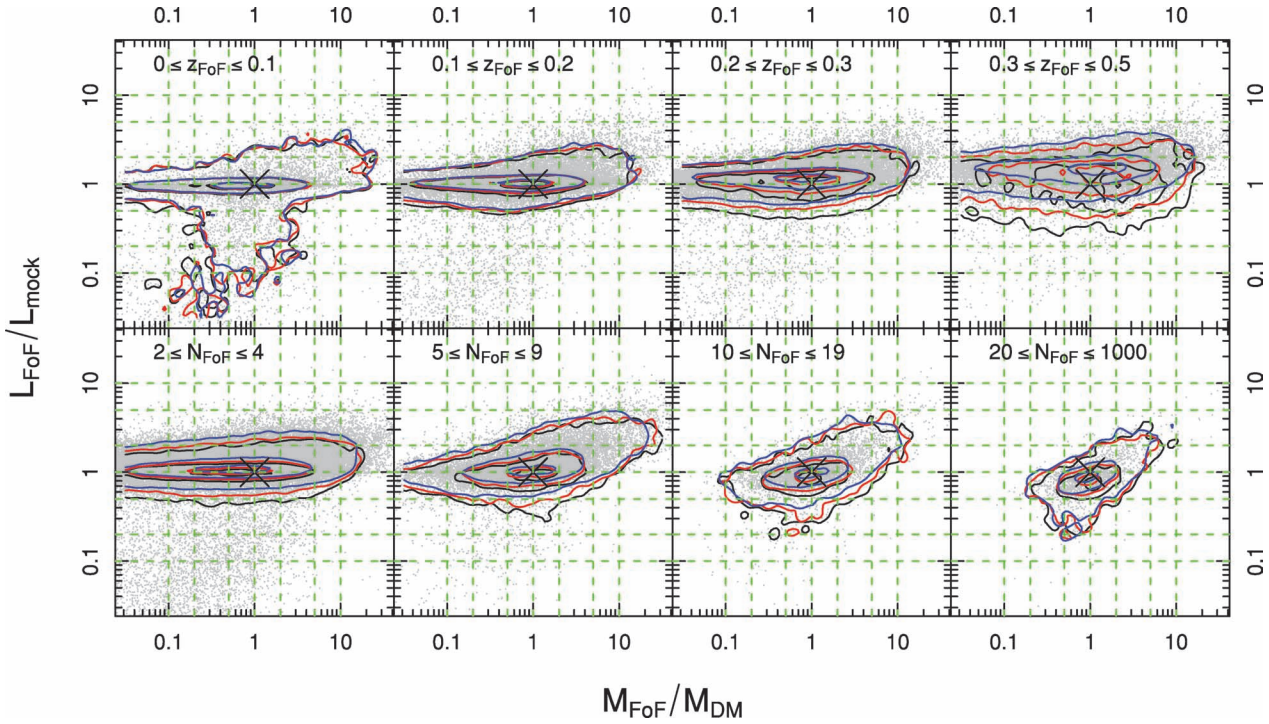

Figure 11. Comparison of the fidelity of the recovered group mass (*x*-axis) against the group luminosity (*y*-axis), split as a function of redshift and multiplicity (top and bottom panel, respectively). For both axes only a global median correction optimized for $N_{\rm FoF} \geq 5$ groups is applied, i.e. we use equations (18) and (22) with $A = 10.0$ and $B = 1.04$ for the mass and luminosity estimates, respectively. The vertical (horizontal) green dashed lines present accuracy factors of 2/5/10 for mass (luminosity) estimates. The contours represent the regions containing 10/50/90 per cent of the data for three different magnitude limits: $r_{\rm AB} \leq 19.0$ (black), $r_{\rm AB} \leq 19.4$ (red) and $r_{\rm AB} \leq 19.8$ (blue).

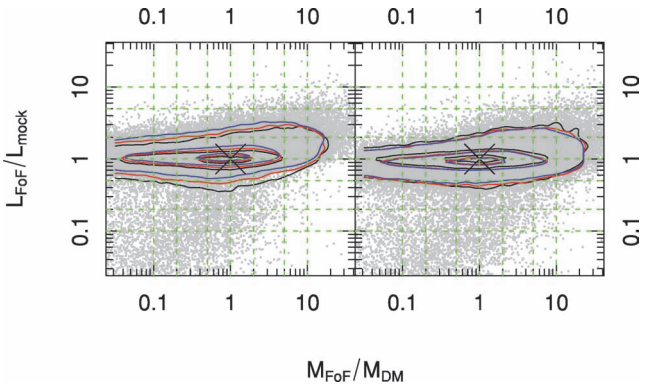

Figure 12. Comparison of the fidelity of the recovered group mass (*x*-axis) against the group luminosity (*y*-axis). The left-hand panel uses only a global median correction for mass and luminosity, optimized for $N_{\rm FoF} \geq 5$ groups (i.e. equations 18 and 22 with $A = 10.0$ and $B = 1.04$). The right-hand panel uses the redshift- and multiplicity-dependent scaling functions of equations (19) and (23) with parameters listed in Tables 4 and 6, respectively. The green dashed lines show measurement accuracy factors of 2/5/10 for the mass and luminosity separately. The contours represent the regions containing 10/50/90 per cent of the data for three different magnitude limits: $r_{\rm AB} \leq 19.0$ (black), $r_{\rm AB} \leq 19.4$ (red) and $r_{\rm AB} \leq 19.8$ (blue).

Figs 13 and 14 show how $Q_{\rm tot}$ and $E_{\rm tot}$ vary within different group subsets for best-matching FoF/halo mock groups. The grouping optimization was not done with the whole sample, rather only groups with $N_{\rm FoF} \geq 5$ contributed to the cost function. Hence panels that contain groups of lower multiplicity (i.e. $2 \leq N_{\rm FoF} \leq 4$) did not drive the optimization, but demonstrate the consequence of it.

The parameter that best constrains the group quality is the multiplicity, where the spread in observed grouping quality reduces for higher multiplicity systems. The most accurate groups tend to be at redshifts $z \sim 0.2$ and have low multiplicities. This is to be expected since the global optimization considered will naturally be drawn to the regime where most groups are. That said, the bijective fraction of recovered groups is best for high-multiplicity systems and remains very steady with redshift. The overall effect is that groups are more likely to be unambiguously discovered (i.e. bijective) when $N_{\rm FoF}$ is high (middle panels of Fig. 14), while the quality of the groups is, on average, quite constant with $N_{\rm FoF}$ (middle panel of Fig. 13). Bijection and quality are obviously related, and these results should be interpreted as low-multiplicity groups possessing a large amount of scatter in the quality of grouping, meaning that they can be scattered below the quality limits required for a successful bijection even though the median quality is quite high. Higher multiplicity systems possess less intrinsic scatter in the quality of grouping, meaning they are very rarely scattered below the bijection limits, and consequently the average bijection fraction remains higher.

The exception to this is that the lowest mass groups appear to be the most accurately recovered, even though most observed have masses $M \sim 10^{13}\,h^{-1}\,{\rm M}_{\odot}$. This can be understood when careful attention is paid to how the FoF algorithm constructs the groups. It creates upper limits for the allowed difference in either the radial (velocity) or tangential (physical) separation between galaxies. It must be the case that groups that are constructed from galaxies that are at the limit of the allowed separations will be larger in terms of projected radius and observed velocity dispersion than groups with galaxy separations well within these limits. This means they will have larger dynamical masses, and assuming interlopers are spread uniformly in space they will have a lower $Q_{\rm tot}$ since they will

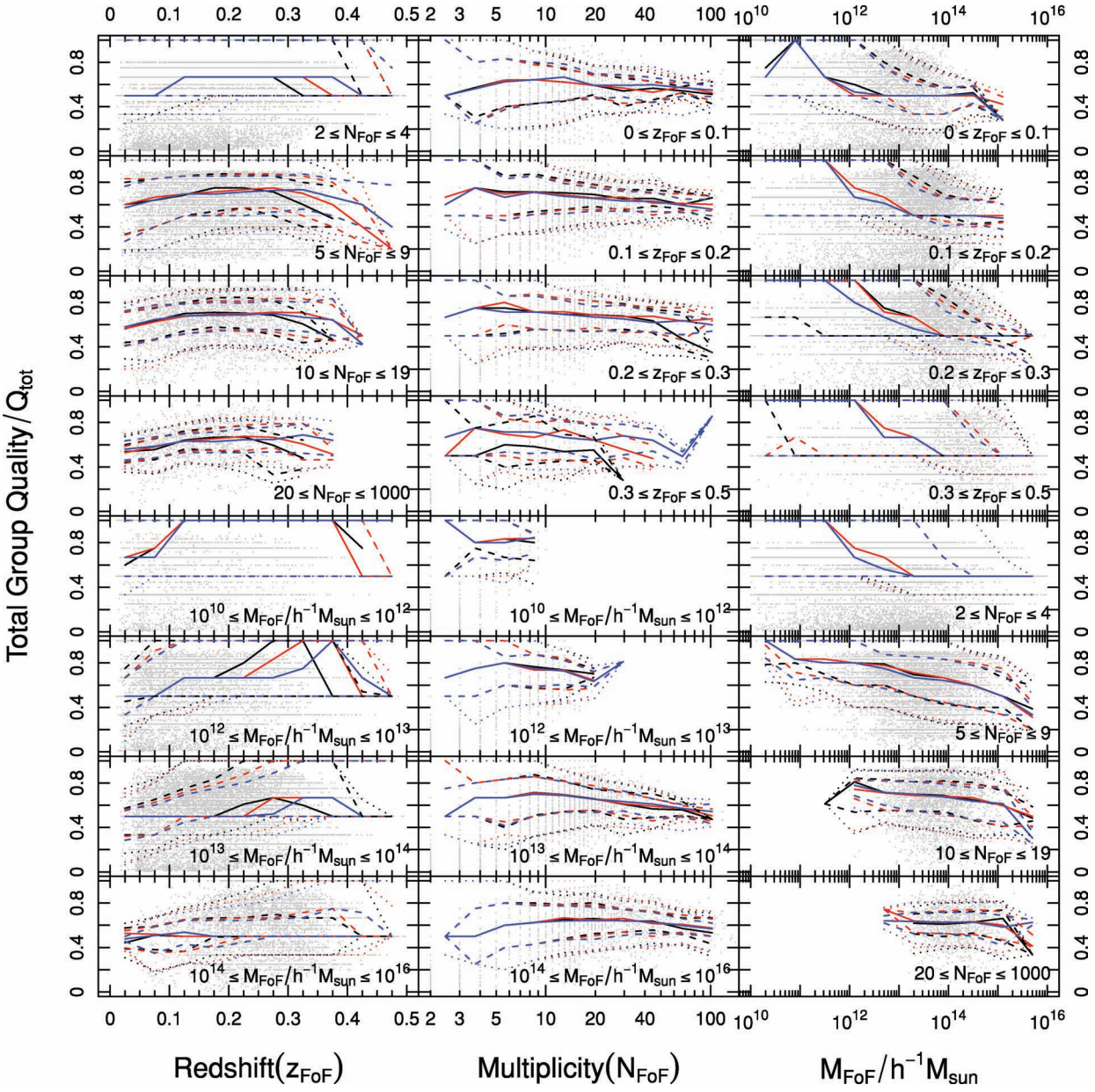

Figure 13. Total group quality ($Q_{\rm tot}$) as a function of group redshift ($z_{\rm FoF}$), group multiplicity ($N_{\rm FoF}$) and group mass ($M_{\rm FoF}$). Each panel presents a specific subsample of groups, as indicated by the key. Solid lines represent the moving median for $r_{\rm AB} \leq 19.0$ (black), $r_{\rm AB} \leq 19.4$ (red) and $r_{\rm AB} \leq 19.8$ (blue) survey limits. Dashed (dotted) lines are for 25 and 75 (10 and 90) percentiles. Grey points show the $r_{\rm AB} \leq 19.4$ data.

cover a larger volume in redshift space, so be more likely to include interlopers. This is an interesting effect of the grouping, because although the masses measured are likely to be too small the actual groups are extremely secure.

With this understandable effect in mind, different methods for estimating the intrinsic $Q_{\rm tot}$ using observed linking characteristics were investigated. The most successful proved to be calculating the following for each group:

$$L_{\rm proj} = \frac{\sum_{i=1}^{N_{\rm FoF}} \sum_{j=1}^{N_{\rm FoF}} \left[1 - \frac{\tan\theta_{i,j}\,(D_{{\rm com},i} + D_{{\rm com},j})}{b_{i,j}\,(D_{{\rm lim},i} + D_{{\rm lim},j})}\,\delta^{c}_{i,j}\right]}{N_{\rm links}}, \qquad (24)$$

where $\delta_{i,j}$ is unity if i and j are directly linked (and zero otherwise), while all other terms are as described in equation (1). Hence the sum is done over allowed links within the group ($N_{\rm links}$) which has a limit of $N_{\rm FoF}(N_{\rm FoF} - 1)$. This statistic estimates how much closer than the allowed maximum separation all of the galaxies are on average, and when this number is large it indicates the group must be very compact in projection relative to the allowed size. Fig. 15 demonstrates how $L_{\rm proj}$ correlates loosely with $Q_{\rm tot}$. Interestingly, the equivalent statistic measuring the radial linking shows very little correlation with $Q_{\rm tot}$. This means that outliers tend to fit quite comfortably in velocity space, but look anomalous in projection. To aid the selection of high-fidelity groups $L_{\rm proj}$ will be released along with the group catalogue.

4.7 Sensitivity of grouping to mock catalogues

So far in this work we have made the implicit assumptions that the mocks are to a large extent a good representation of the real Universe and that optimizing the grouping algorithm to recover mock groups

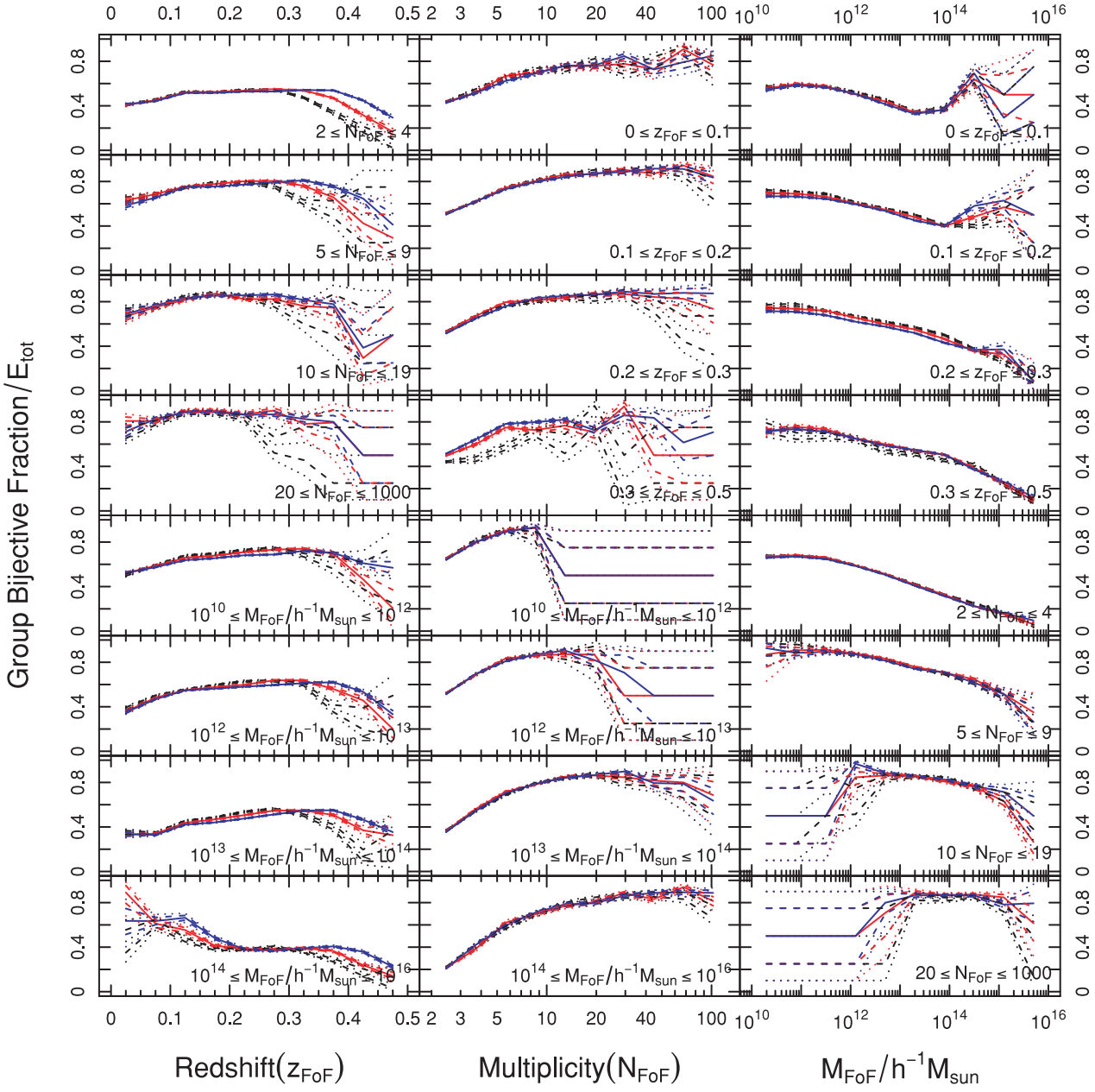

Figure 14. Bijective group fraction ($E_{\rm tot}$) as a function of group redshift ($z_{\rm FoF}$), group multiplicity ($N_{\rm FoF}$) and group mass ($M_{\rm FoF}$). Each panel presents a specific subsample of groups, as indicated by the key. Solid lines represent the moving median for $r_{\rm AB} \leq 19.0$ (black), $r_{\rm AB} \leq 19.4$ (red) and $r_{\rm AB} \leq 19.8$ (blue) survey limits. Dashed (dotted) lines are for 25 and 75 (10 and 90) percentiles. Grey points show the $r_{\rm AB} \leq 19.4$ data.

as accurately as possible will have the desired effect of also returning the best groups from the GAMA data. Clearly we should be wary of the effects of overtuning our algorithm to the mocks, especially given the limitations listed in Section 2.3. To better understand how sensitive our final group catalogue might be to certain intrinsic mock properties, three small variations affecting the redshift-space positions of the mock galaxy were implemented which lead to slight changes in the 'observed' mocks. These perturbations where applied to the $r \leq 19.4$ mock catalogues since that should be indicative of the impact we might expect. The modifications consist of

(1) increasing all galaxy peculiar velocities along the line of sight by 10 per cent, creating groups that are less compact in velocity space than the default mocks: mock$_+$;

(2) reducing all galaxy peculiar velocities along the line of sight by 10 per cent, creating groups that are more compact in velocity space than the default mocks: mock$_-$;

(3) convolving all galaxy peculiar velocities along the line of sight with a Gaussian velocity distribution of width $\sigma = 50\,{\rm km\,s^{-1}}$, mimicking the GAMA velocity errors: mock$_\sigma$.

The first two sets of mock, mock$_+$ and mock$_-$, test the sensitivity of the grouping to the fidelity in which small-scale redshift-space distortions are accounted for in the mocks. From Kim et al. (2009) and Norberg et al. (in preparation) we know that the Bower et al. (2006) semi-analytic galaxy formation model do not reproduce very accurately the redshift-space clustering on h^{-1} Mpc scales and smaller. By systematically modifying the peculiar velocities by ± 10

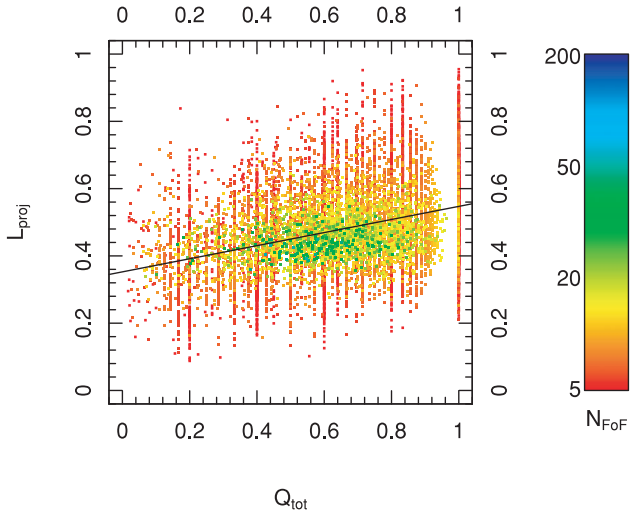

Figure 15. Comparison of the observed linking strength $L_{\rm proj}$ with the intrinsic group quality $Q_{\rm tot}$. The colour of each data point represents the group multiplicity, going from $N_{\rm FoF} = 5$ (red) to 200 (blue). The correlation is strongest for low-multiplicity systems, which is important since it is these that can be pathologically bad. The black line is the linear regression fit to the entire data, so it predominantly describes the lower multiplicity systems.

per cent and by keeping the same FoF grouping parameters we attempt to address this mismatch between data and mocks and measure how sensitive the grouping is such differences. From Norberg et al. (in preparation) we expect that an additional velocity bias of $\sim +10$ per cent to the mock galaxies should be enough to reconcile the redshift-space clustering of the mocks and the data. The third set, mock$_\sigma$, tests the sensitivity of the grouping to velocity errors, which were not considered in the nominal mocks described in Section 2.3 but clearly present in the GAMA data. To fully simulate how we treat the errors for the real GAMA data the velocity errors are taken off in quadrature as described in equation (17).

The FoF algorithm with the nominal parameters as listed in Table 1 is applied to the three sets of mocks. The FoF grouping of the standard and modified mocks results in pretty similar findings: the first impact these perturbed mocks might have on the grouping is on the group assignments themselves, so $S_{\rm tot}$ was calculated for all three varieties of new mocks where the reference mock data is now the original mock lightcone. This means we are only analysing how similar the new mock FoF groupings are to the original set, not to the 'true' mock groupings. $S_{\rm tot}$ is found to be $\sim$0.97 for all three varieties of mock perturbation for $N_{\rm halo} \geq 2$, and only drops slightly for $N_{\rm halo} \geq 20$ which shows the greatest discrepancy. In this regime mock$_+$ has $S_{\rm tot} = 0.94$, mock$_-$ has $S_{\rm tot} = 0.96$ and mock$_\sigma$ has $S_{\rm tot} = 0.93$.

For the estimated masses, it is obvious that mock$_-$ and mock$_+$ will require slightly different scaling relations to recover unbiased halo masses. The global mass scaling factor (where $N_{\rm FoF} \geq 5$) for mock$_-$, A_-, needs to be 11.6, so 16 per cent larger than A, while A_+ needs to be $\sim$8.7, so 15 per cent smaller than A. This implies that we have an underlying systematic uncertainty of at least 15 per cent on all masses assuming we expect the true physics to vary the galaxy velocities at the 10 per cent level. Naively we might have expected the difference to be at the $\sim$20 per cent level since $1.1^2 = 1.21$, but the random nature of peculiar velocities and the slight variation in grouping conspires to reduce the variation.

For mock$_\sigma$ we require exactly the same global scaling relation as before, i.e. $A_\sigma = A = 10.0$. This implies that removing the velocity error in quadrature is the correct procedure, and means we certainly do not expect the uncertainty in radial velocities to have a significant effect on the implied masses.

The implication for the group luminosities is, as expected, very marginal with respect to these modifications of the mocks, which is a result of the grouping still being rather good for all three set of mocks (as evidenced by the marginal change in $S_{\rm tot}$) despite the algorithm not being tuned to them.

5 GLOBAL PROPERTIES OF G^{3}CV1

Having run extensive optimizations and calculated refinements based on the mock catalogues, the algorithm was run over the real GAMA data. In total, taking the deepest version of each GAMA survey region possible, 14 388 groups were formed containing 44 186 galaxies out of 110 192 galaxies in our volume-limited selection, meaning 40 per cent of all galaxies are assigned to a group. This is almost identical to the average grouping rate found in the mocks, also 40 per cent.

The headline group number statistics are listed in Table 7 for each of the GAMA regions, i.e. G09, G12 and G15. $r_{\rm AB} \leq 19.0$ and $\leq$19.4 catalogues were made for G09, G12 and G15, and an extra $r_{\rm AB} \leq 19.8$ catalogue was created for G12 (the only region that has deep enough spectroscopy). This table also includes the expectation from the mocks with the minimum and maximum numbers of groups in the nine GAMA lightcone mocks. Subsets that have numbers that are outside the min–max range of the mocks are flagged with an asterisk.

From Table 7 we conclude that for most multiplicity ranges and survey limits the number of GAMA groups detected is very comparable to the predictions from the GAMA lightcones. Over the full GAMA lightcones G12 and G15 are very close to the mean counts recovered from the mocks whilst G09, although very much at the underdense extreme, is not outside the min–max range expected. The comparison between data and mocks seems less favourable when splitting the groups by redshift and survey depth, where five GAMA subsets lie outside of the min–max limits of the mocks. The difference becomes less and less significant the deeper the survey is and seems to be most significant in G09, which is underdense in all subsets investigated.

It is well established that G09 is underdense below $z < 0.2$ compared to the whole of SDSS (Driver et al. 2011), whilst G12 and G15 are closer to the large-scale average. Overall, this underdensity accounts for why we find fewer groups in G09. G09 is similar to the most underdense and group sparse GAMA area found in the mocks, suggesting it is a rare event in the mocks but at least not completely unmatched. G12 is most like the typical mock distribution, and the GAMA $r_{\rm AB} \leq 19.8$ group catalogue is the most similar to the mocks of all catalogues. This catalogue tends to contain fewer large multiplicity groups than predicted by the mocks. These inconsistencies are not highly significant overall, but they reflect similar findings in the 2PIGG catalogue (Eke et al. 2004a).

Fig. 16 shows the position of the GAMA groups in redshift space projected on to the equatorial plane, with the symbol size reflecting the group multiplicity and colour the group velocity dispersion. The highest multiplicity groups are at lower redshifts, as should be expected in an apparent magnitude limited sample. This figure particularly highlights the sample variance seen between regions, as already mentioned in the discussion of Table 7. There are vast regions of space that contain massive clusters and an assortment of groups, overlapping so tightly as to produce patches of solid colour in the plot. However, between these large filamentary regions there

Table 7. Number of galaxy groups as a function of multiplicity, redshift and survey depth. The GAMA groups are split by GAMA regions, i.e. G09, G12 and G15. For the mocks, the mean number of groups between all nine mock GAMA lightcones in a single GAMA region of $\sim$48 deg^2 is listed together with their low and high extreme across all mocks (within brackets). Samples with an asterisk are those which are outside the min–max range of the mocks.

	$r \leq 19.0$				$r \leq 19.4$				$r \leq 19.8$	
	G09	G12	G15	Mocks (low, high)	G09	G12	G15	Mocks (low, high)	G12	Mocks $\pm \sigma$ (low, high)
$N_{\rm group}$ 2–4	2051	2409	2436	2334 (3154, 4100)	3334	3703	3776	3623 (3154, 4100)	5687	5520 (4861, 6101)
$N_{\rm group}$ 5–9	190	233	234	253 (188, 294)	329	395	339	390 (322, 455)	539	584 (509, 661)
$N_{\rm group}$ 10–19	45	55	59	66 (43, 82)	75	79	102	102 (69, 133)	121	155 (98, 189)
$N_{\rm group}$ 20+	8*	16	16	26 (15, 39)	17*	26	25	40 (20, 55)	44	62 (34, 88)
$z_{\rm group}$ 0–0.1	419	577	512	531 (318, 856)	514	705	597	634 (379, 1028)	857	746 (437, 1204)
$z_{\rm group}$ 0.1–0.2	973	1369	1450*	1144 (803, 1381)	1338	1829	1967*	1552 (1076, 1841)	2331	2024 (1424, 2424)
$z_{\rm group}$ 0.2–0.3	725	640	633	814 (606, 996)	1372	1217	1198	1377 (1074, 1683)	1997	2124 (1683, 2584)
$z_{\rm group}$ 0.3–0.5	178	127	100*	189 (125, 258)	531	452	480	593 (421, 730)	1206	1426 (1044, 1708)
Total	2294	2713	2745	2678 (2204, 3107)	3755	4203	4242	4156 (3578, 4728)	6391	6321 (5535, 7025)

are voids that, whilst still possessing galaxies (in lower densities), barely contain a single significant group. At low redshifts ($z < 0.1$) where the mean galaxy number density is the highest, such voids are still very evident in the GAMA data.

We still see groups of significant size ($N_{\rm FoF} \sim 20$) beyond a redshift of 0.3 in G09, and there is evidence of filamentary structure in the underlying galaxy population beyond $z \sim 0.4$ in G12 (G12 being 0.4 mag deeper than G09/G15 probes structure to slightly higher redshifts). In G12 there are a number of low-multiplicity systems beyond a redshift of 0.4 – these groups appear to be associated with nodes in filamentary structure and have been visually identified as large clusters. This means that GAMA is able to measure the evolution of group properties and filamentary structure over a redshift baseline of 0–0.5, which is $\sim$5 Gyr, or 36 per cent the lifetime of the Universe – an evolutionary time-span for large-scale structure analysis that is unprecedented in a single coherent survey.

Fig. 17 shows a series of 1° wide declination slices in G12 that cover $0.15 \leq z_{\rm group} \leq 0.2$. The black points show the location of individual galaxies, and as expected the groups closely trace overdensities seen in the galaxy distribution. Intriguingly, we see evidence of extremely fine filamentary structure that is not associated with any of the defined groups. If these structures were purely radial in direction, then they could be claimed as misidentified systems, for which the filamentary structure merely betrays the velocity dispersion along the line of sight. Instead we witness gentle sweeping arcs that move round steadily radially and in projection, implying that they are real fine filamentary structure that connects group nodes. This is probably one of the first times that one sees the galaxy distribution mimicking so closely the filamentary distribution which is so commonly seen in large DM-dominated numerical simulations.

The most striking of these filaments can be found in the top right-hand panel of Fig. 17 where fine strands can be seen extending out from $\alpha \sim 180°$ and $z \sim 0.18$, and also from $\alpha \sim 182°$ and $z \sim 0.19$. In both of these cases it is possible to identify group and cluster nodes that connect the filaments together, but there are no groups detected within the filaments themselves. It is important to highlight that without GAMA redshifts these regions would have previously been identified as void like, and that the additional galaxies are not randomly distributed 'field' galaxies, but appear to be in extremely well-defined environments, but non-grouped with respect to the GAMA mean galaxy number density.

After considering the spatial distribution of GAMA galaxy groups, Fig. 18 shows the distributions of four basic properties of the G^3Cv1: the observed group multiplicity, mass, velocity dispersion and radius distributions. We now discuss them in turn.

The top left-hand panel of Fig. 18 presents the distribution of group multiplicities for three survey depths (coloured solid lines) to be compared to the equivalent average mock multiplicity distributions (dashed lines). Unsurprisingly the raw number of groups increases with survey depth explaining why the three coloured curves are ordered as a function of survey depth, i.e. $r_{\rm AB} \leq 19.0$ (black), $r_{\rm AB} \leq 19.4$ (red) and $r_{\rm AB} \leq 19.8$. More importantly, the number of high-multiplicity systems is significantly different between data and mocks, a result already discussed in Table 7, while their numbers are much more similar for low-multiplicity systems. The difference at the high-multiplicity end is important and put key constraints on the galaxy formation model used. The group multiplicity distribution is mostly sensitive to the Halo Occupation Distribution (HOD), as for a given number of haloes the group multiplicity distribution is entirely dependent on its HOD. A known feature of the GALFORM Bower et al. (2006) galaxy formation model is its tendency to populate the more massive haloes with an excess of faint satellite galaxies (e.g. Kim et al. 2009).

The top right-hand panel of Fig. 18 presents the distribution of group masses for three survey depths (coloured solid lines) to be compared to the equivalent average mass distributions from the mocks (dashed lines). For the comparison to be as fair as possible, the group masses used for the mocks are estimated in exactly the same way as the data. Because velocities uncertainties have not been included in the mocks it is essential to remove from this comparison all groups which velocity dispersion estimate is significantly affected by this uncertainty, as the group mass is proportional to σ^2 (see equation 18) and would bias the distribution. To achieve this we simulated mock σ groups with 80 km s^{-1} velocity error and calculated the velocity dispersion at which more than 95 per cent of the population should be robust to being scattered below the presumed GAMA group velocity error (which would give a corrected σ of 0 km s^{-1}). This velocity dispersion limit was found to be 130 km s^{-1}. Thus the top right-hand panel only shows a comparison of groups where this selection has been applied.

The agreement between data and mocks beyond $\sim 10^{13}\, h^{-1}\, {\rm M}_\odot$ is remarkably good for all survey depths, with possibly only the normalization that is slightly lower for GAMA data than for the mocks (however within the typical scatter expected from sample variance). The relative profiles are all very similar. We note that this mass distribution has been convolved with the error distribution on the group masses which have been estimated using a single

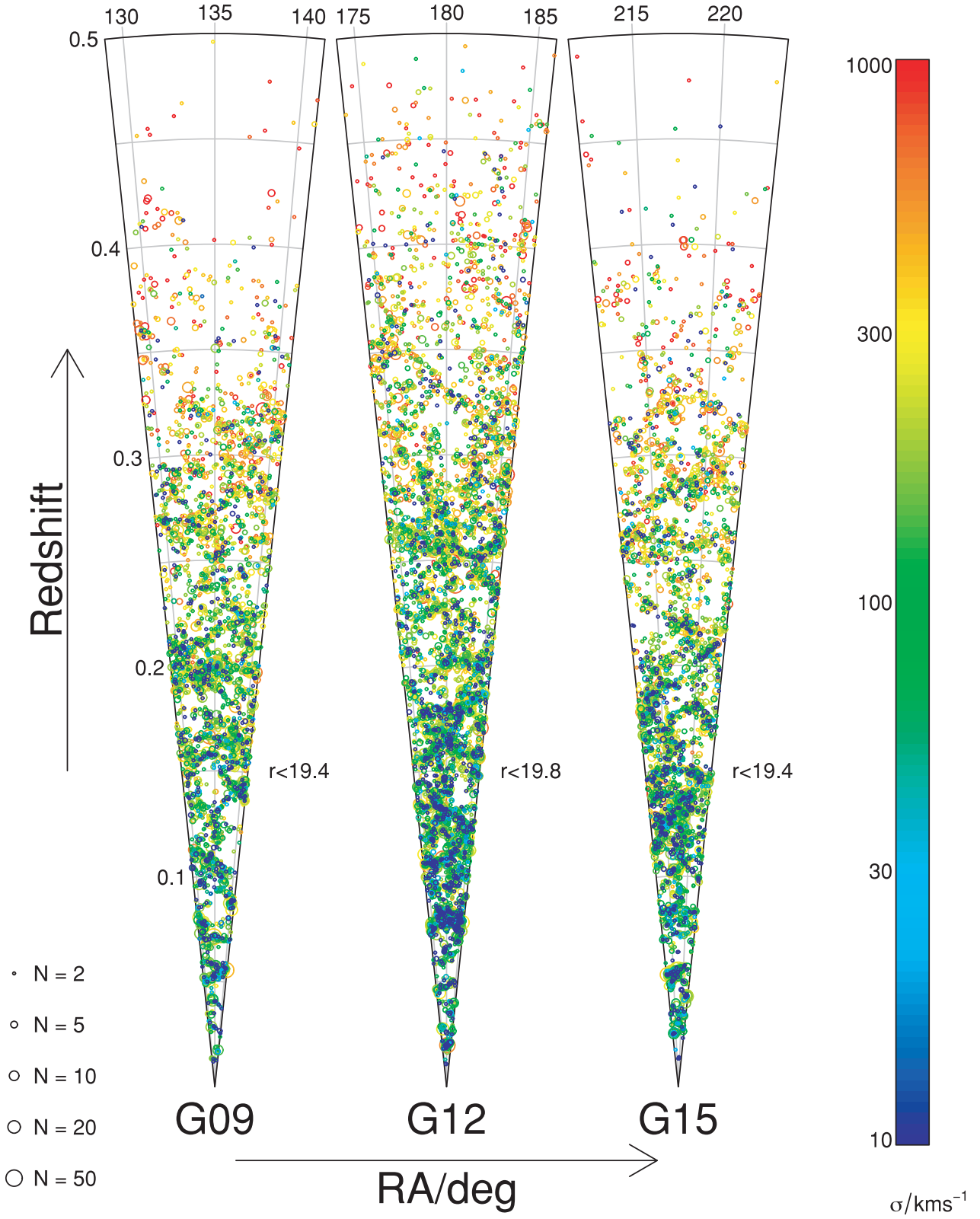

Figure 16. Redshift-space position of GAMA galaxy groups projected on to the equatorial plane, split by survey area and with symbol size reflecting the group multiplicity and symbol colour the group velocity dispersion (see figure keys for exact values). G09 and G15 are for a survey depth of $r_{AB} \leq 19.4$, while G12 is for $r_{AB} \leq 19.8$, explaining why the number of groups detected at higher redshifts is larger in G12 compared to G09 and G15. At low redshifts where the projection effects are the smallest, groups are still visually strongly associated with the filaments and nodes of the larger scale cosmic structure. Fewer groups are found beyond at higher redshift, a result of GAMA survey being magnitude limited.

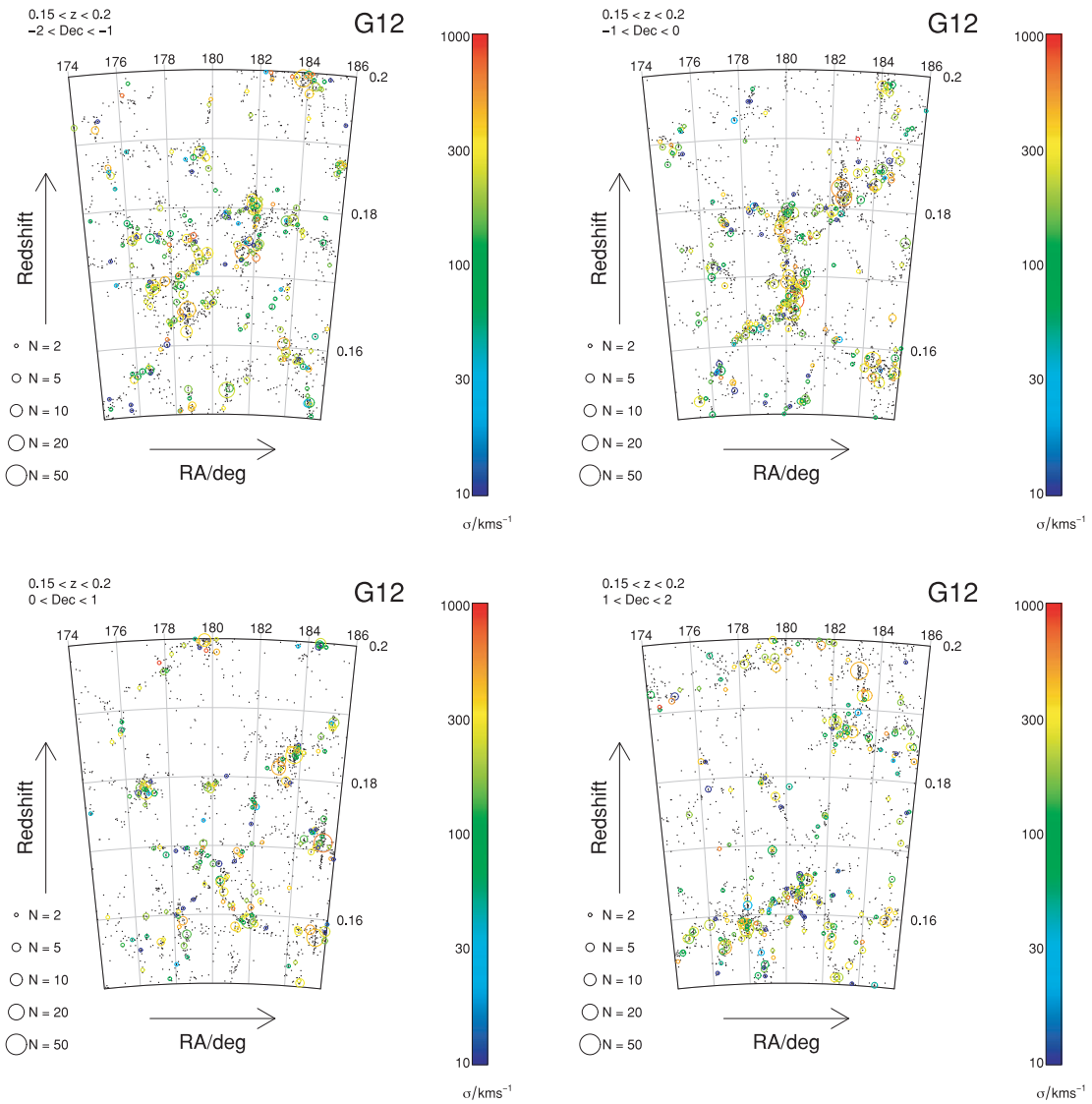

Figure 17. Four 1° wide declination slices of the GAMA G12 region covering the $0.15 < z < 0.20$ redshift range. Declination increases from left to right and top to bottom, as indicated by the panel key. Galaxies are shown with black dots, and galaxy groups with the same symbols as in Fig. 16.

correction factor ($A = 10$). This explains why unrealistically large-group masses are found (e.g. greater than $10^{16}\,h^{-1}\,\mathrm{M}_{\odot}$). More detailed work on estimating the group masses is underway (Alpaslan, in preparation).

The bottom left-hand panel of Fig. 18 presents the distribution of group velocity dispersions for three survey depths (coloured solid lines) to be compared to the equivalent average group velocity dispersion distributions from the mocks (dashed lines). For the comparison to be as fair as possible, the velocity dispersion used for the mocks is estimated in exactly the same way as the data. Because velocities uncertainties have not been included in the mocks, it is essential to remove from this comparison all groups those for which the velocity dispersion estimate is significantly affected by this uncertainty. This can be straightforwardly done by ignoring groups with $\sigma \leq 130\,\mathrm{km\,s^{-1}}$ (as discussed above). Beyond that limit in the velocity dispersion distribution, the data and mock distributions are very comparable, showing yet again how closely matched the mocks and the data are. For smaller velocity dispersion system a more careful modelling of the velocity errors (and hence velocity dispersion errors) is needed before any conclusions can be drawn on how appropriate the mocks are. Work is currently ongoing within GAMA to better understand the precise nature, and distribution, of the redshift velocity errors. A full comparison is deferred until these errors have been fully characterized.

Finally, the bottom right-hand panel of Fig. 18 presents the distribution of group radius for three survey depths (coloured solid lines) to be compared to the equivalent average group radius distributions from the mocks (dashed lines). Considering the full sample of groups, the mocks and the data seem to be very comparable.

To investigate in more detail where differences between the GAMA data and the mocks may reside we divided the mass, velocity dispersion and radius distributions into multiplicity subsets (Fig. 19). For clarity, Fig. 19 only uses the $r_{\mathrm{AB}} \leq 19.4$ survey limit, the deepest limit appropriate for all GAMA regions. Furthermore, mock distributions for each of the nine mock lightcones are shown with grey lines rather than the sample mean shown in Fig. 18. This makes allows us to see where the GAMA group distributions lie in the context of the full range of mock distributions, and therefore

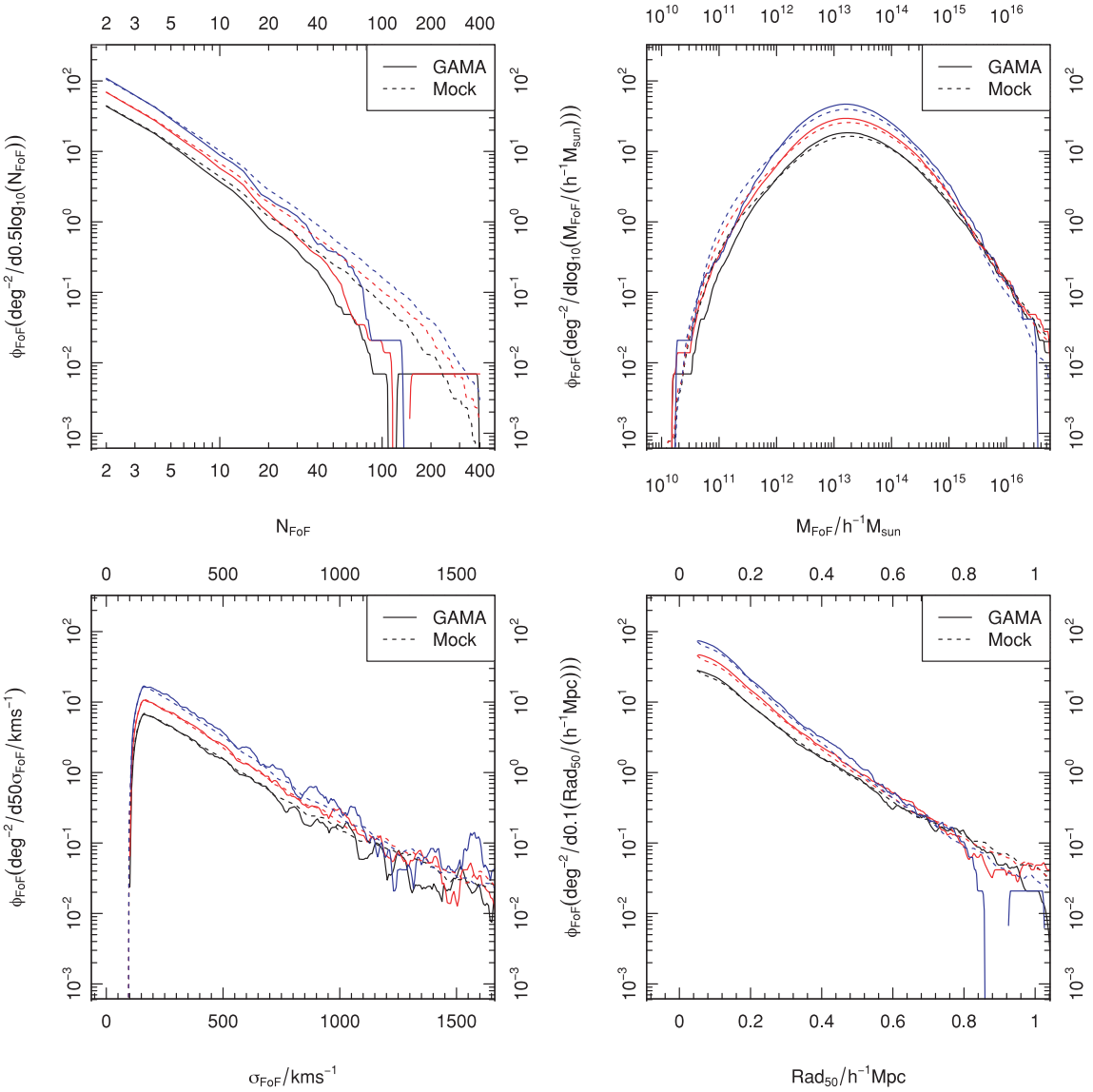

Figure 18. Global group properties of the G^{3}Cv1 compared to the corresponding mock group catalogue: group multiplicity distribution (top left), dynamical group mass distribution limited to $\sigma_{\rm FoF} \geq 130\,{\rm km\,s^{-1}}$ (top right), group velocity dispersion distribution limited to $\sigma_{\rm FoF} \geq 130\,{\rm km\,s^{-1}}$ (bottom left) and group radius distribution (bottom right). Solid (dashed) lines for GAMA (mock) for $r_{\rm AB} \leq 19.0$ (black), $r_{\rm AB} \leq 19.4$ (red) and $r_{\rm AB} \leq 19.8$ survey limits. The denominator shown in the y-axis is the bin width applied, so numbers quoted are per the stated denominator. See text for discussion.

how significant the differences are as a function of each parameter. Plotting in this manner makes comparison much clearer than showing the error bars. The agreement is very good for $2 \geq N_{\rm FoF} \geq 4$ for all three group properties plotted, however, discrepancies are apparent for higher multiplicities both in normalization and to a lesser extent in shape.

For the mass distributions (top panel of Fig. 19) it is clear that GAMA possesses a lower normalization in counts compared to the mock groups, an effect that is more noticeable for larger multiplicities. The largest deviations in the shapes of the distribution are seen for $M_{\rm FoF} \leq 10^{13}\,{\rm M}_{\odot}$, where we see excess number counts for the mock groups. This difference is most evident for $5 \geq N_{\rm FoF} \geq 9$. The most likely explanation for this low mass excess comes from the finding that mock groups are typically more compact than GAMA groups, which will naturally cause a lower estimation of the mass. The radial discrepancies are discussed in more detail below.

The velocity dispersion (middle panel of Fig. 19) only shows strong evidence of a normalization offset, where the agreement is excellent for low-multiplicity systems but as this increases we find the GAMA groups have a general count deficit. Since the strength of the normalization offset varies with multiplicity the difference cannot be simply due to sample variance, where all multiplicity subsets would betray the same deficit.

The differences between GAMA and the mocks are most pronounced for the group radius (bottom panel of Fig. 19). The most significant deviations are seen where ${\rm Rad}_{50} \leq 0.2\,h^{-1}$ Mpc: GAMA finds many fewer systems, and the effect is much more significant for higher multiplicities where the mocks contain a significant excess of compact systems not seen at all in the data. At the GAMA median redshift ($z \simeq 2$), $0.1\,h^{-1}$ Mpc (comoving) radius corresponds to an angular separation of 25 arcsec on the sky. Whilst the simplest explanation might be the GAMA survey suffers from significant

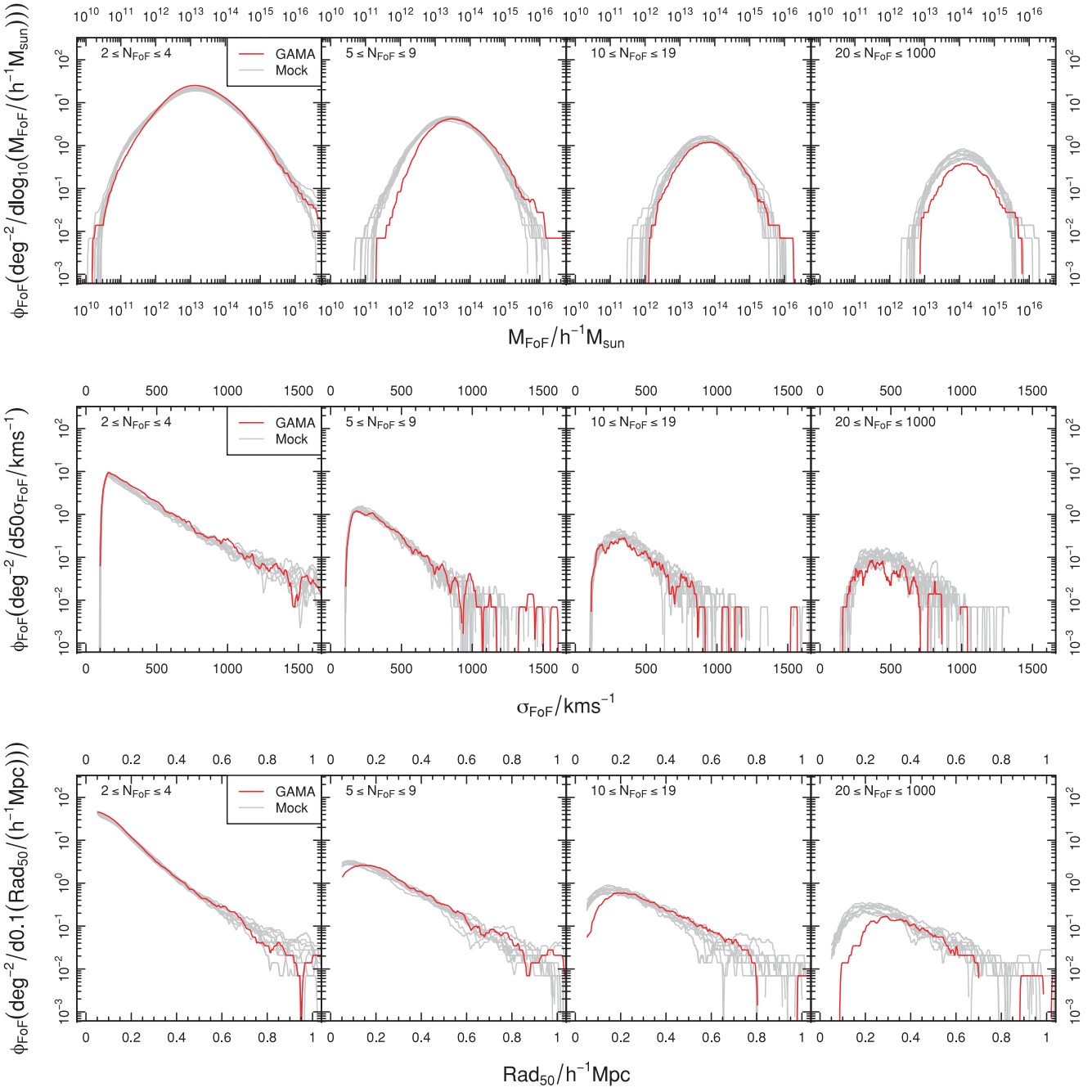

Figure 19. Distribution of GAMA and mock galaxy group mass (top panels), velocity (middle panels) and radius (bottom panels) for a survey depth of $r_{\rm AB} \leq 19.4$. GAMA is shown in red while the mocks are in grey. Multiplicity subsets are as stated in each panel. For the mass and velocity panels the mocks and GAMA data are limited to $\sigma \geq 130\,{\rm km\,s^{-1}}$, required to avoid the effects of velocity errors in the GAMA data biasing the results. For the mass and velocity plots the clearest differences are normalization offsets, and for $N_{\rm FoF} \geq 5$ there is a clear tendency for GAMA groups to have smaller $M_{\rm FoF}$ and $\sigma_{\rm FoF}$ for a given multiplicity subset. The distributions are significantly different for compact systems ($\rm Rad_{50} \leq 0.2\,\mathit{h}^{-1}\,Mpc$) with $N_{\rm FoF} \geq 5$, where GAMA groups are less compact in projection. This effect becomes more significant for higher multiplicity subsets.

close pair incompleteness, fig. 19 of Driver et al. (2011) suggests this not be the case: GAMA is better than 95 per cent complete for systems with up to five neighbours within 40 arcsec (on the sky). These separations are much larger than the expected optical confusion limit (1–2 arcsec), so photometric bias (i.e. close pairs not being deblended) cannot explain the discrepancies we find. Since the main variance witnessed for velocity dispersions between the mocks and GAMA data is the normalization, the more compact mock groups appear to be the origin of the low-mass population we find in the top panels of Fig. 19.

The differences seen in Fig. 19 could well be due to limitations in the physics implemented in the GALFORM Bower et al. (2006) semi-analytic galaxy formation model, where the exact distribution of galaxies within a halo depends on their dynamical friction time-scale and which DM particle the galaxy was originally associated with. Despite the high numerical resolution of the Millennium

Simulation, the vast majority of the satellite galaxies in the galaxy formation model are not resolved in subhaloes, implying that their merging time-scales are governed by an analytic calculation and their position is given by the most bound DM particle of their parent halo. A consequence of a too long merging time-scale is an overabundance of galaxies at small distances away from the centre of the halo. This, together with the definition of group radius adopted for this work (i.e. Rad_{50}), is the most likely explanation for the apparent excess of compact groups in the mocks compared to the data. This has the consequence of also creating a deficit of low-mass groups in the GAMA data in comparison to the mocks since the dynamical masses are directly proportional to the group radius measured.

In summary, the G^{3}Cv1 and its mock counterpart are similar in many respects, but not all. In the discussion of Figs 18 and 19 it has become clear that already G^{3}Cv1 is providing new constraints to the galaxy formation model used to construct the mocks and will be implemented in the next generation of mocks. Investigating the discrepancies between GAMA and mock group catalogues, and the impact this has on any measured HMF, is a complex and important task. A full analysis is deferred to a GAMA paper in preparation, which will present a more in depth analysis of a series of statistically equivalent mocks as well as galaxy-formation-based mocks as used here. Only with a large variety of mocks will it be possible to put realistic constraints on the underlying DM model. The analysis in the present paper is entirely limited to one family of mock realizations, which explains why the constraints from the GAMA groups are so far mostly limited to possible constraints on the galaxy formation model rather than on the underlying DM physics.

6 GROUP EXAMPLES

For every group we create a rgb image as a $K_{\mathrm{AB}} - r_{\mathrm{AB}} - u_{\mathrm{AB}}$-band composite, along with visual diagnostics that allow interesting features to be easily identified. Example images are shown in Figs 20–22 and discussed hereafter.

Fig. 20 highlights four cluster-scale groups extracted from the GAMA data. The top panel shows relatively low-redshift clusters with high multiplicities, whilst the bottom panels are examples of low-multiplicity groups that show evidence for a lot of associated galaxies that are fainter than the GAMA survey limits (shown by a dashed red line on the luminosity distribution plotted in each panel). All of these groups are quite circularly symmetric and concentrated towards the centre, both of which are indicators of a well virialized population of galaxies.

Fig. 21 shows groups at radically different stages of evolution. The top panels show examples of fossil groups with one exceptionally dominant BCG. In both cases only the BCG had a known redshift before GAMA, and the large peak in the redshift distribution suggests particularly strong radial linking – an indication that the grouping is reliable. The bottom panels show groups with very loose association in comparison. Both groups are quite massive (in the cluster regime) and have identifiable background galaxies, but neither exhibits a centrally concentrated distribution of galaxies or a dominant BCG. Both of these groups have a relatively uniform redshift distribution, showing none of the strong central peak seen for the fossil groups in the top panel. The bottom right-hand group in particular has a very flat luminosity distribution and an extremely non-circular distribution of galaxies. The most likely scenario is that this group has two distinct substructures (top and bottom) collapsing into each other, where the bottom structure is physically nearer to us in space and thus exhibits a large extra component of recessional velocity towards the CoM.

Fig. 22 shows particularly pleasing examples of galaxy–galaxy merging/interactions. A natural outcome from the GAMA group catalogue is that nearly all possible close pairs will be grouped (modulo a very small amount of incompleteness). Often these merging systems will be found in higher multiplicity systems, but here are examples of two member groups that exhibit evidence for mergers. The top left- and top right-hand panels show quite similar looking systems: a red (likely passive) galaxy interacting with a blue (late-type) galaxy. The top left-hand panel has larger tidal tails and more of the flux is in the late-type system, suggesting it is at an early stage of the merging process. The top panels are examples where the multipass nature of GAMA has overcome the problems of fibre collisions to give us redshifts for both galaxies in the merging system. The bottom panels show merging systems that are both too faint and too close to be obtainable with SDSS data. The bottom left-hand panel system appears to be a triple merger system, where the blue galaxy to the right does not have GAMA redshift because it is too faint. The bottom right-hand panel shows two extremely faint and relatively u-band bright galaxies merging – a tidal connection can be seen between them. In both of these bottom panels the groups in question have extremely low velocity dispersions ($\sim$45 km s^{-1}) and very low implied dynamical masses ($\sim 10^{10}\,h^{-1}\,\mathrm{M}_{\odot}$).

In such systems dynamical friction is acting in such a manner that the dynamical mass will likely not be a good indicator of the intrinsic halo mass, rather it highlights a system where the energy has been transferred from group scale kinematics (energy in galaxies) to galaxy scale kinematics (energy in the stars/gas). Dynamical friction conspires to reduce the velocity difference and physical distance between merging galaxies, and since we use $M_{\mathrm{FoF}} \propto \sigma^2 R$ this will also reduce the implied dynamical mass that we measure.

6.1 GAMA group catalogues

The generation of a group catalogue produces a myriad of outputs, most of which are not of interest to the typical user. To ease interpretation for the average user, a deliberately simplified set of outputs will be made available. For each GAMA region two tables are released. The first one is a two-column link list that identifies which group every galaxy belongs. The second is a table of group properties with the most important attributes of each group. This includes the group radius Rad_{50}, the velocity dispersion σ_{FoF} and the implied dynamical mass.

Other metrics related to each group are also calculated to aid the analysis and interpretation of individual grouping quality. As well as the L_{proj} linking quality discussed above, the kurtosis of the radial separation of all galaxies from the group centre is calculated and the 'modality' of the system is also computed using $(1 + \mathrm{skewness}^2)/(3 + \mathrm{kurtosis}^2)$. This will be 1/3 for a normal distribution and 0.555 for a uniform, and is a useful metric since it does not just provide information on how non-Gaussian the velocity profile of each system is – it also provides information on the whether the velocity profile is more cusped or cored than a Gaussian distribution. Additionally, in a similar manner to how the local overdensity was calculated in a comoving cylinder centred around each galaxy, the local relative density is calculated for each group. This is calculated using a comoving cylinder of radius $1.5\,h^{-1}$ Mpc and total radial depth of $36\,h^{-1}$ Mpc, and gives a measure of how isolated the groups are relative to much larger scale structure.

Finally, as a separate but useful output from creating the G^{3}Cv1, a full pair catalogue will be released. This is a natural output of

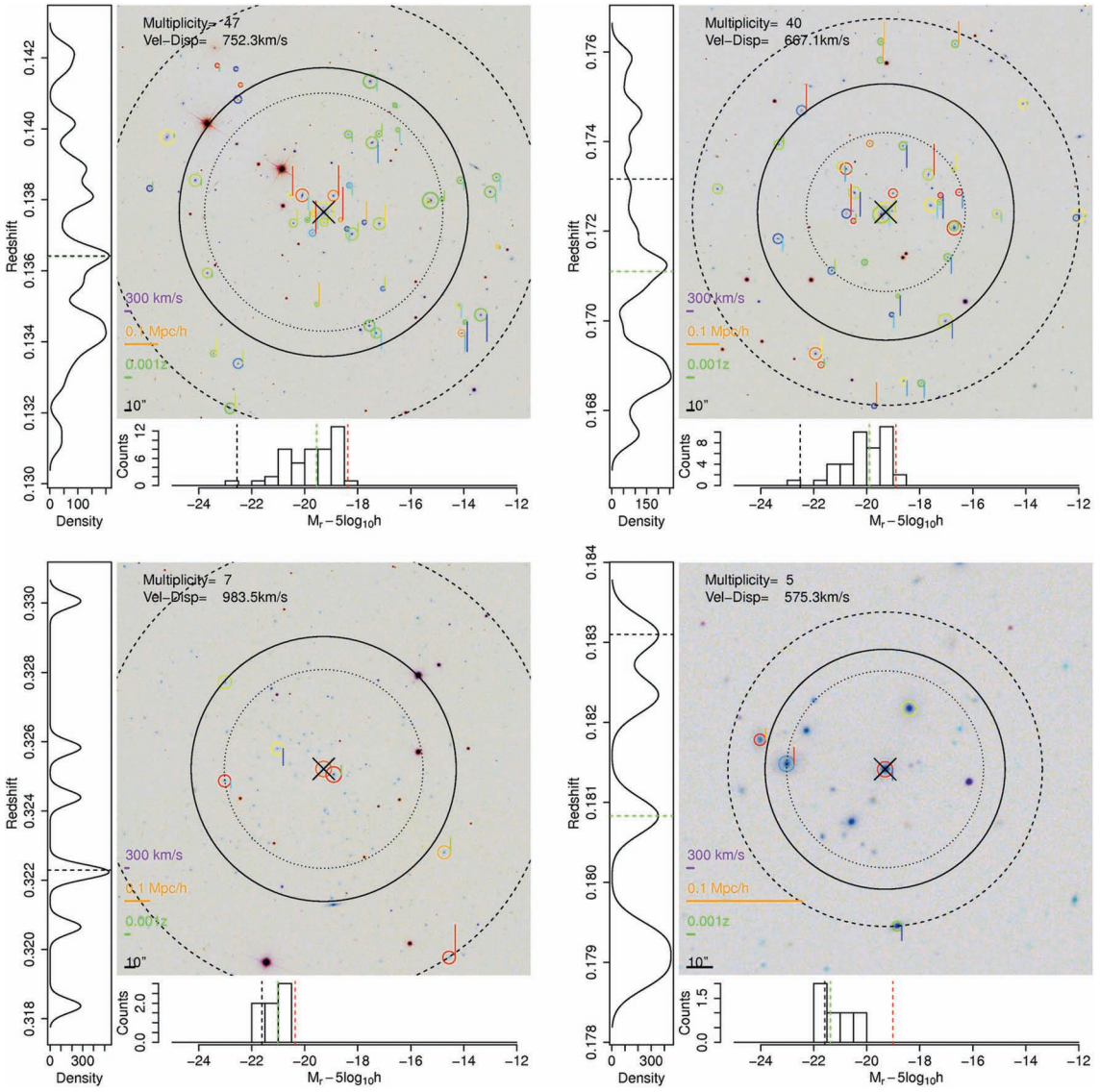

Figure 20. Top panels show two cluster scale groups confirmed spectroscopically. Bottom panels show low-multiplicity groups with significant, possibly associated, background galaxies. The rgb image is a K_{AB}–r_{AB}–u_{AB}-band composite. The size of the circle marking group members scales with the r_{AB}-band flux and its colour reflects the galaxy $u_{AB} - r_{AB}$ colour. A galaxy redshifted with respect to the group median redshift has a red upwards pointing line which length scales with the velocity difference, while for a blueshifted one the line is blue and points downwards. The rings represent the 50th, 68th and 100th percentiles of the radial galaxy distributions relative to the iterative group centre. The velocity PDF smoothed with a Gaussian kernel of width $\sigma = 50\,\mathrm{km\,s^{-1}}$ (the typical GAMA velocity error) is shown on the left of each panel, where the group median is shown with a green dashed line and the BCG with a black dashed line. The bottom plot presents the raw absolute r_{AB} magnitude distribution of the group, with the effective GAMA survey limit shown with a red dashed line, the group median absolute magnitude with green and the BCG absolute magnitude with black.

the galaxy–galaxy linking stage of the grouping algorithm, and includes all pairs that are within a common velocity separation of $1000\,\mathrm{km\,s^{-1}}$ and a physical projected separation of $50\,h^{-1}$ kpc. This will be used within the team for work involving the study of galaxy pairs.

7 CONCLUSIONS

In this paper we have presented a new group catalogue based on the spectroscopic component of the GAMA survey. The FoF-based grouping algorithm used has been extensively tested on semi-analytic derived mock catalogues, and has been designed to be extremely robust to the effects of outliers and linking errors. The velocity dispersion and radius of the groups are median unbiased, even when allowing for the possibility of catastrophic grouping errors. Globally, 77 per cent of the recovered FoF groups bijectively (unambiguously) match a mock group, and 89 per cent of all mock groups are bijectively recovered. The purity of all FoF groups is 80 per cent, and for mock groups the equivalent figure is 73 per cent. This suggests that the FoF algorithm is quite well balanced and does not have a strong preference to overgrouping or to conservatively recovering just the strongly bound core of systems.

The overall number of groups within from $0 \leq z \leq 0.5$ is remarkably consistent between the mocks and real groups, and for the most part comfortably within the range expected given the large sample variance that can affect galaxy surveys such as GAMA. The histograms of raw group multiplicity and dynamically estimated group mass show a large amount of agreement between the

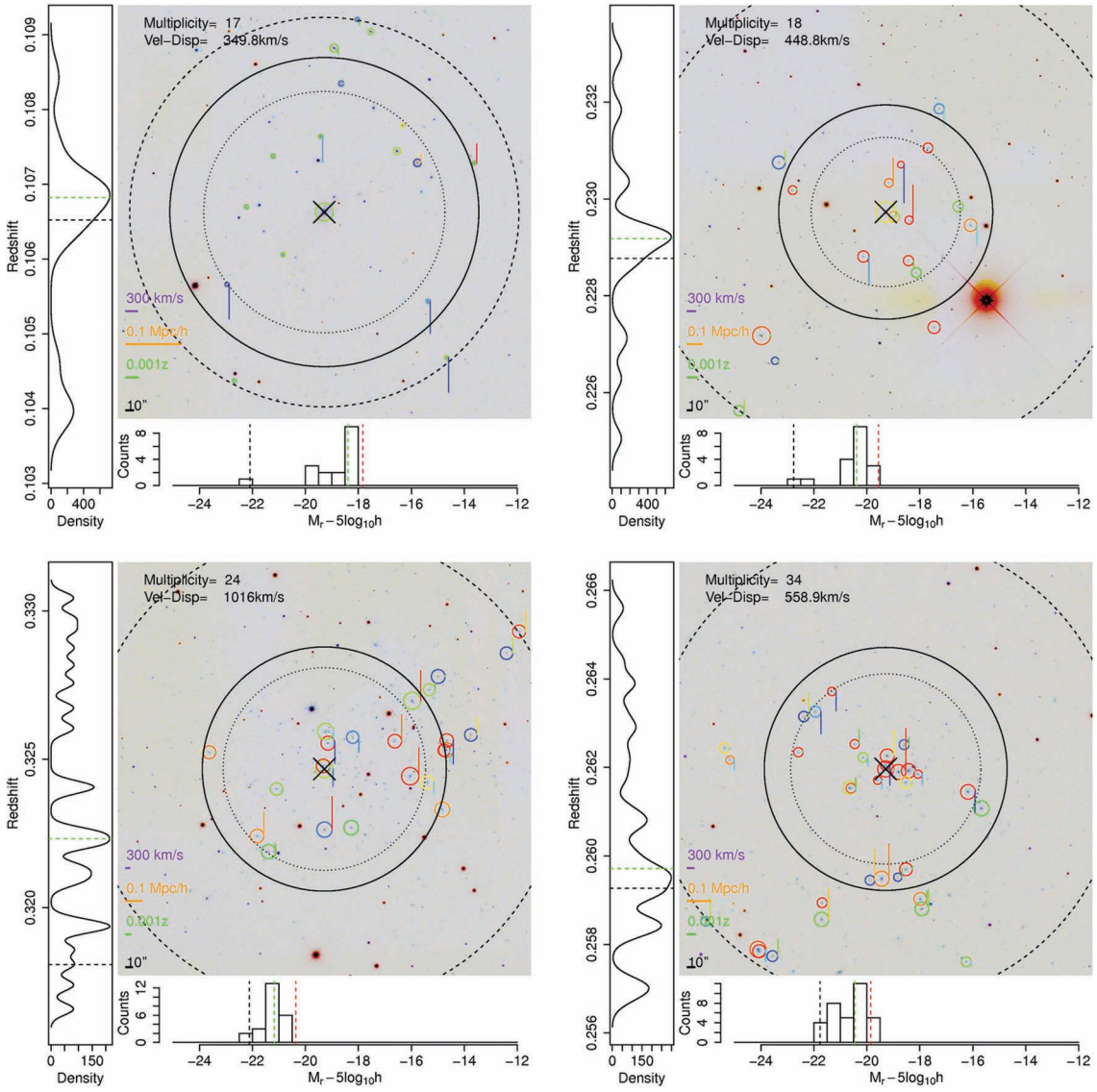

Figure 21. Top panels are potential fossil groups, where the BCG is at least 2 mag brighter than the second ranked galaxy in the r_{AB} band (in the case of the top right-hand groups the second rank galaxy is nearer in magnitude than this, but it is separated a large distance in projection). Bottom panels show groups with complex in-fall structure. See Fig. 20 for figure description.

GAMA data and the mock catalogues for the most part. Discrepancies appear at the high-multiplicity end, where GAMA finds fewer high-multiplicity systems than recovered from the mock volumes. A more in depth analysis of the discrepancies between GAMA and mock groups is deferred to a later paper, still in preparation.

The showcase examples of a small number of GAMA groups highlight the parameter space that is now opened up, and demonstrate the advantages brought by having extremely high spatial completeness. Accurate group dynamics and a full sample of close pairs will be of key importance for determining the HMF in upcoming work, and for finding new constraints on the galaxy merger rate in the local Universe, two of the main goals of the GAMA survey.

The G^3Cv1 will be made publicly available on the GAMA website (http://www.gama-survey.org) as soon as the associated redshift data are made available. Interested parties should contact the author at asgr@st-and.ac.uk if they wish to make use of the group catalogue data before the full public release.

ACKNOWLEDGMENTS

We thank Vincent Eke for his helpful refereeing comments. These added clarity to various aspects of the paper. ASGR acknowledges STFC and SUPA funding that was used to do this work. PN acknowledges a Royal Society URF, an ERC StG grant (DEGAS-259586) and STFC funding. GAMA is a joint European–Australasian project based around a spectroscopic campaign using the Anglo-Australian Telescope. The GAMA input catalogue is based on data taken from the Sloan Digital Sky Survey and the UKIRT Infrared Deep Sky Survey. Complementary imaging of the GAMA regions is being obtained by a number of independent survey programs including *GALEX* MIS, VST KIDS, VISTA VIKING, *WISE*, Herschel-ATLAS, GMRT and ASKAP providing UV to radio coverage. GAMA is funded by the STFC (UK), the ARC (Australia), the AAO and the participating institutions. The GAMA website is http://www.gama-survey.org/.

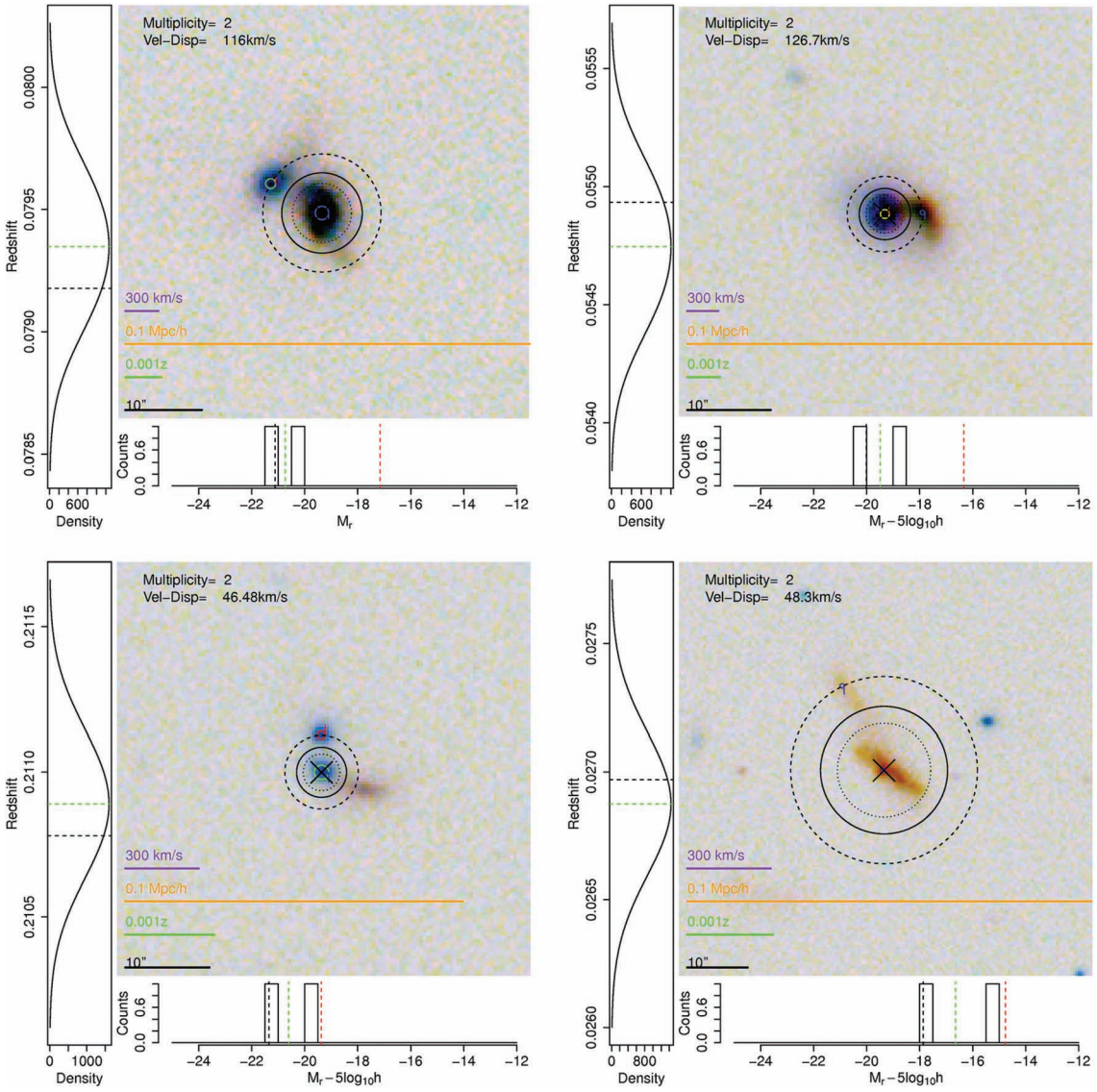

Figure 22. Examples of ultra low-mass groups that are also excellent candidates for merging systems. The bottom plots are groups that are within the nominal SDSS $r_{AB} \leq 17.77$ limit, but one or both galaxies are missing from that survey due to fibre collisions. The bottom plots are groups that are both too faint and too close together to be present in a spectroscopic SDSS catalogue. See Fig. 20 for figure description.

REFERENCES

Abell G. O., 1958, ApJS, 3, 211
Baldry I. K. et al., 2010, MNRAS, 404, 86
Beers T. C., Flynn K., Gebhardt K., 1990, AJ, 100, 32
Benson A. J., Bower R. G., 2010, MNRAS, 405, 1573
Berlind A. A. et al., 2006, ApJS, 167, 1
Blanton M. R., Roweis S., 2007, AJ, 133, 734
Blanton M. R. et al., 2003, ApJ, 592, 819
Bower R. G., Benson A. J., Malbon R., Helly J. C., Frenk C. S., Baugh C. M., Cole S., Lacey C. G., 2006, MNRAS, 370, 645
Brough A., Duncan A. F., Virginia A. K., Warrick C., 2006, MNRAS, 370, 1223
Chilingarian I. V., Mamon G. A., 2008, MNRAS, 385, 83
Cole S., Lacey C. G., 1996, MNRAS, 281, 716
Cole S., Lacey C. G., Baugh C. M., Frenk C. S., 2000, MNRAS, 319, 168
Colless M., Dalton G., Maddox S., Sutherland W., Norberg P., 2001, MNRAS, 328, 1039
Cooray A., 2006, MNRAS, 365, 842
Cooray A., Sheth R., 2002, Phys. Rep., 372, 1
Croton D. J. et al., 2005, MNRAS, 356, 1155
De Vaucouleurs G., 1975, in Sandage A., Sandage M., Kristian J., eds, Galaxies and the Universe. Chicago Univ. Press, Chicago, p. 557
Driver S. P. et al., 2011, MNRAS, 413, 971
Efstathiou G., Ellis R. S., Peterson B. A., 1988, MNRAS, 232, 431
Eke V. R., Cole S., Frenk C. S., 1996, MNRAS, 282, 263
Eke V. R. et al., 2004a, MNRAS, 348, 866
Eke V. R. et al., 2004b, MNRAS, 355, 769
Gerke B. F. et al., 2005, ApJ, 625, 6
Helly J. C., Cole S., Frenk C. S., Baugh C. M., Benson A. J., Lacey C. G., 2003, MNRAS, 338, 903
Huchra J. P., Geller M. J., 1982, ApJ, 257, 423
Jenkins A., Frenk C. S., White S. D. M., Colberg J. M., Cole S., Evrard A. E., Couchman H. M. P., Yoshida N., 2001, MNRAS, 321, 372
Kim H. S., Baugh C. M., Cole S., Frenk C. S., Benson A. J., 2009, MNRAS, 400, 1527
Knobel C. et al., 2009, ApJ, 697, 1842
Lin H., Yee H. K. C., Carlberg R. G., Morris S. L., Sawicki M., Patton D. R., Wirth G., Shepherd C. W., 1999, ApJ, 518, 533

Loveday J., Maddox S. J., Efstathiou G., Peterson B. A., 1995, ApJ, 442, 457
Moore B., Frenk C. S., White S. D. M., 1993, MNRAS, 261, 827
Navarro J., Frenk C. S., White S. D. M., 1996, ApJ, 462, 563
Nelder J. A., Mead R., 1965, Comput. J., 7, 308
Norberg P. et al., 2002, MNRAS, 336, 907
Plionis M., Basilakos S., Ragone-Figueroa C., 2006, ApJ, 650, 770
Robotham A., Wallace C., Phillipps S., De Propris R., 2006, ApJ, 652, 1077
Robotham A., Phillipps S., De Propris R., 2008, ApJ, 672, 834
Robotham A. et al., 2010a, Publ. Astron. Soc. Australia, 27, 76
Robotham A., Phillipps S., De Propris R., 2010b, MNRAS, 403, 1812
Springel V., White S. D. M., Tormen G., Kauffmann G., 2001, MNRAS, 328, 726
Springel V. et al., 2005, Nat, 435, 629
Yang X., Mo H. J., van den Bosch F. C., 2003, MNRAS, 339, 1057
Yang X., Mo H. J., van den Bosch F. C., Jing Y. P., 2005, MNRAS, 356, 1293
Zwicky F., Herzog E., Wild P., 1961, Catalogue of Galaxies and of Clusters of Galaxies, Vol. I. California Institute of Technology (CIT), Pasadena

This paper has been typeset from a TEX/LATEX file prepared by the author.